

Earthquake-swarms, slow-slip and fault-interactions at the western-end of the Hellenic Subduction System precede the Mw 6.9 Zakynthos Earthquake, Greece

Vasiliki Mouslopoulou¹, Gian Maria Bocchini², Simone Cesca³, Vasso Saltogianni³, Jonathan R Bedford³, Gesa Maria Petersen³, Michael Gianniou⁴, and Onno Oncken³

¹Institute of Geodynamics, National Observatory of Athens

²Ruhr University Bochum

³GFZ German Research Centre for Geosciences

⁴University of West Attica

November 24, 2022

Abstract

The month-to-year-long deformation of the Earth's crust where active subduction zones terminate is poorly explored. Here we report on a multidisciplinary dataset that captures the synergy of slow-slip events, earthquake swarms and fault-interactions during the ~5 years leading up to the 2018 M 6.9 Zakynthos Earthquake at the western termination of the Hellenic Subduction System (HSS). It appears that this long-lasting preparatory phase initiated due to a slow-slip event that lasted ~4 months and released strain equivalent to a ~M 6.3 earthquake. We propose that the slow-slip event, which is the first to be reported in the HSS, tectonically destabilised the upper 20-40 km of the crust, producing alternating phases of seismic and aseismic deformation, including intense microseismicity ($M < 4$) on neighbouring faults, earthquake swarms in the epicentral area of the M 6.9 earthquake ~1.5 years before the main event, another episode of slow-slip immediately preceding the mainshock and, eventually, the large (M6.9) Zakynthos Earthquake. Tectonic instability in the area is evidenced by a prolonged (~4 years) period of overall suppressed b-values (< 1) and strong earthquake interactions on discrete strike-slip, thrust and normal faults. We propose that composite faulting patterns accompanied by alternating (seismic/aseismic) deformation styles may characterise multi-fault subduction-termination zones and may operate over a range of timescales (from individual earthquakes to millions of years).

1 **Earthquake-swarms, slow-slip and fault-interactions at the western-end of the**
2 **Hellenic Subduction System precede the M_w 6.9 Zakynthos Earthquake, Greece**

3
4 **Vasiliki Mouslopoulou^{1,3*}, Gian-Maria Bocchini², Simone Cesca³, Vasso Saltogianni³,**
5 **Jonathan Bedford³, Gesa Petersen³, Michael Gianniou^{4,5}, Onno Oncken³**
6

7 ¹National Observatory of Athens, Institute of Geodynamics, Athens, 11810, Greece

8 (vasiliki.mouslopoulou@noa.gr)

9 ²Ruhr University of Bochum, Institute of Geology, Mineralogy and Geophysics, Germany

10 (Gian.Bocchini@rub.de)

11 ³GFZ Helmholtz Centre Potsdam, German Research Centre for Geosciences, Telegrafenberg
12 14473 Potsdam, Germany

13 (cesca@gfz-potsdam.de; salto@gfz-potsdam.de; jbed@gfz-potsdam.de; gesap@gfz-potsdam.de;
14 oncken@gfz-potsdam.de)

15 ⁴Hellenic Cadastre, Athens, 15562, Greece (mgianniu@ktimatologio.gr)

16 ⁵University of West Attica, Athens, 12243, Greece (mgianniou@uniwa.gr)

17 *Corresponding author: Vasiliki Mouslopoulou (vasiliki.mouslopoulou@noa.gr)
18

19 **Key Points:**

- 20 • First ever report of slow-slip event in the Hellenic Subduction System prior to a M_w 6.9
21 event
- 22 • Synergy of upper-plate faulting, slow-slip & earthquake-swarms tectonically destabilise a
23 subduction-termination prior to the mainshock
- 24 • Alternating phases of seismic and aseismic slip at various depths accommodates plate-
25 motion at the western Hellenic Subduction System
26

27 **Abstract**

28 The month-to-year-long deformation of the Earth's crust where active subduction zones
29 terminate is poorly explored. Here we report on a multidisciplinary dataset that captures the
30 synergy of slow-slip events, earthquake swarms and fault-interactions during the ~5 years
31 leading up to the 2018 M_w 6.9 Zakynthos Earthquake at the western termination of the Hellenic
32 Subduction System (HSS). It appears that this long-lasting preparatory phase initiated due to a
33 slow-slip event that lasted ~4 months and released strain equivalent to a ~ M_w 6.3 earthquake. We
34 propose that the slow-slip event, which is the first to be reported in the HSS, tectonically
35 destabilised the upper 20-40 km of the crust, producing alternating phases of seismic and
36 aseismic deformation, including intense microseismicity ($M < 4$) on neighbouring faults,
37 earthquake swarms in the epicentral area of the M_w 6.9 earthquake ~1.5 years before the main
38 event, another episode of slow-slip immediately preceding the mainshock and, eventually, the
39 large (M_w 6.9) Zakynthos Earthquake. Tectonic instability in the area is evidenced by a
40 prolonged (~4 years) period of overall suppressed b-values (< 1) and strong earthquake
41 interactions on discrete strike-slip, thrust and normal faults. We propose that composite faulting
42 patterns accompanied by alternating (seismic/aseismic) deformation styles may characterise
43 multi-fault subduction-termination zones and may operate over a range of timescales (from
44 individual earthquakes to millions of years).

45

46 **Keywords:** Hellenic subduction, slow-slip, upper-plate, microseismicity, Zakynthos, plate-
47 interface

48

49 **1 Introduction**

50 Well-monitored examples of large-magnitude earthquakes that rupture subduction plate-
51 boundaries reveal that these earthquakes may be preceded by episodes of slow-slip, swarm
52 activity and/or large foreshocks (i.e. Kato et al., 2012; Bouchon et al., 2013; Schurr et al., 2014).
53 Examples that document such interactions, most of which have been operating on the plate-
54 interface, include the 2011 M_w 9 Tohoku-Oki Earthquake in Japan, the 2012 M_w 7.6 Nicoya
55 Peninsula Earthquake in Costa Rica, and the 2014 M_w 8.1 Iquique megathrust earthquake in
56 Chile (Kato et al., 2012; Schurr et al., 2014; Ruiz et al., 2014; Davis et al., 2015; Uchida et al.,

57 2016). The interrelation, and possible interdependence, of these deformational processes is
58 nevertheless poorly understood, especially in circumstances where upper-plate faulting
59 accommodates a significant percentage of the plate-motion, with the plate-interface playing a
60 secondary role (i.e. Wallace et al., 2012; Cesca et al., 2017). Such settings are often encountered
61 at the terminations of subduction zones (Mouslopoulou et al., 2019), where plate-motion
62 transitions from thrust to strike-slip faulting, producing complex kinematic patterns in the
63 overriding plate (Mann and Frohlich, 1999). The characteristics (duration, size, distribution) of
64 the interplay between the various types of deformation (seismic vs aseismic) along subduction
65 terminations, especially prior or immediately after large-magnitude earthquakes, is poorly
66 explored mainly due to the lack of relevant data.

67 The M_w 7.8 Kaikoura Earthquake, that ruptured the southern-end of the Hikurangi margin
68 in 2016 (Cesca et al., 2017), to-date provides the only well-monitored example of a large-
69 magnitude earthquake that ruptured a subduction termination (Mouslopoulou et al., 2019). This
70 earthquake enhanced our understanding of seismogenesis along subduction terminations, as it
71 demonstrated that earthquake-rupture involved primarily (~80%) slip on upper-plate faults, with
72 only weak seismic-slip and aseismic afterslip on the plate-interface (Mouslopoulou et al., 2019).

73 On October 25th, 2018 a M_w 6.9 earthquake ruptured the western termination of the
74 Hellenic Subduction System (HSS) across a zone where plate-motion transitions from mainly
75 thrust to mainly strike-slip faulting (Royden and Papanikolaou, 2011), providing a valuable new
76 case-study of a well-monitored earthquake that ruptures a subduction termination (Fig. 1). This
77 earthquake, that occurred southwest of the island of Zakynthos (Sokos et al., 2020) (Fig. 1), was
78 preceded by a 5-year-long tectonic instability in the broader epicentral area of the M_w 6.9 event
79 and an intense aftershock sequence (Figs 2 and 3). Here, we report on a multidisciplinary dataset
80 of seismological, geodetic, seismic-reflection and bathymetric information that, collectively,
81 capture the earthquake and fault kinematics within this earthquake sequence (hereafter refer to as
82 the Zakynthos Earthquake Sequence - ZES), prior to and after the main event. We find that
83 alternating phases of aseismic and seismic deformation on the subduction-thrust and the
84 overriding plate, respectively, preceded the M_w 6.9 event and accounted for at least 15% of the
85 relative Eurasian/African plate-motion. The aftershock sequence was accommodated by thrust,
86 strike-slip, and normal faulting in the upper-plate (<20 km) and accounted for ~75% of the plate
87 convergence.

88 **2 The kinematics of the western HSS and the M_w 6.9 Zakynthos Earthquake**

89 In the eastern Mediterranean, the oceanic African Plate is being obliquely subducted along
90 the Hellenic margin beneath the continental Eurasian Plate at rates ranging from ~ 26 to 34
91 mm/yr (McClusky et al., 2000) (Fig. 1). At its western-end the subduction system terminates
92 against the dextral Kefalonia Transform Fault (Louvari et al. 1999; Sachpazi et al. 2000),
93 transferring its relative plate-motion onto the Apulian collision front (Pérouse et al., 2017) (Fig.
94 1). The kinematic transition from nearly orthogonal convergence (in the south) to pure strike-slip
95 (in the north) is accommodated, along a ~100 km wide zone offshore from western Peloponnese,
96 by strike-slip, thrust and normal faulting (Fig. 1). The faults presented in Figure 1 are derived
97 from a combination of published information (Kokinou et al., 2005; Kokalas et al., 2013; Makris
98 and Papoulia, 2014; Wardell et al., 2014), analysis of bathymetric data ([https://portal.emodnet-](https://portal.emodnet-bathymetry.eu/?menu=19)
99 [bathymetry.eu/?menu=19](https://portal.emodnet-bathymetry.eu/?menu=19)) and re-interpretation of four (Z207, KY301, Z151AB, KY311 and
100 KY209; for location see Fig. 1) published Multi-channel seismic reflection profiles (Kokalas et
101 al., 2013; Wardell et al., 2014) (Fig. 4).

102 Beneath western Peloponnese the top of the plate-interface lies at depths between 20-40
103 km and has an average dip of ~17° (Pearce et al., 2012; Halpaap et al., 2018, 2019) (Figs. 1 and
104 3). Just southwest of Zakynthos and proximal to the region of the 2018 mainshock, the plate-
105 interface lies at ~15 km depth (Clément et al., 2000), with a series of east-dipping thrust faults
106 displacing the upper section (<15 km) of the crust and the sea-bed (Louvari et al. 1999; Sachpazi
107 et al. 2000; Wardell et al., 2004; Kokinou et al. 2005). Low-dipping reverse faulting in the area is
108 also supported by moment tensors of instrumental seismicity (i.e. Anderson and Jackson, 1987).
109 On the hangingwall of these thrust faults, numerous normal faults have been identified to
110 displace post-Miocene deposits down to depths of at least 10 km (Kokalas et al, 2013; Wardell et
111 al., 2014; this study) (Fig. 4).

112 The 2018 Zakynthos mainshock ruptured the upper <20 km of the crust as a result of
113 shallow thrust and moderately dipping dextral strike-slip faulting (Haddad et al., 2020; Sokos et
114 al., 2020). The focal mechanism presents a large non-double-couple (non-DC) component with a
115 large negative CLVD indicating a complex rupture process (Sokos et al., 2020). The Global
116 Centroid Moment Tensor (Global CMT) project suggests a centroid depth for this event of ~12
117 km and a total seismic-moment release of 2.32×10^{19} Nm (Dziewonski et al., 1981; Ekström et al.,
118 2012). Three past earthquakes with sizes and focal mechanisms similar to that recorded in 2018,

119 have ruptured the crust proximal to Zakynthos over the last ~60 years (in 1959, 1976 and 1997;
120 <http://bbnet.gein.noa.gr/HL/>). The orientation of their focal mechanisms (Kiratzi and Louvari,
121 2003; Sokos et al., 2020) is in agreement with the plate-convergence (Fig. 1), indicating that
122 these earthquakes accommodated a fraction of the relative African-Eurasian plate-motion. No
123 events greater than M7 have been recorded in the ZES region instrumentally or historically
124 (Papazachos and Papazachou, 2003).

125 **3 The 2014-2019 Zakynthos Earthquake Sequence (ZES)**

126 **3.1 Sequence characteristics**

127 The earthquake sequence analysed here (lon: 19.5°E to 21.6°E / lat: 36.8°N to 38°N)
128 derives from the Hellenic Unified Seismological Network (HUSN; <http://bbnet.gein.noa.gr/HL/>)
129 and includes data from the stations of the National Observatory of Athens (NOA), the University
130 of Patras (UP), the Aristotle University of Thessaloniki (AUTH) and eight additional seismic
131 stations deployed in western Peloponnese immediately after the mainshock. The ZES extends
132 over an area of ~18,000 km², from northwest Peloponnese to the west of the islands of
133 Zakynthos and Kefalonia (Figs 1 and 3), and spans a time-period of ~5 ½ years (January 1st,
134 2014 to May 31st, 2019) (Fig. 2a). The ZES includes >12,000 earthquakes (Table S3), with the
135 largest event (M_w 6.9) having occurred ~40 km southwest of the island of Zakynthos on October
136 25th, 2018 (22:54 UTC) due to oblique-thrust faulting (Fig. 1; Table S4). About one third of the
137 events in the ZES occurred prior to the mainshock while two thirds were aftershocks (Figs 2 and
138 3). The majority of these earthquakes have magnitudes below 3.5 (Fig. 2a). The magnitude of
139 completeness (M_c) in the ZES prior to the mainshock is 2.0±0.1, it abruptly increases to 3.5 after
140 the mainshock (Fig. 2b) while it returns to pre-mainshock values (~2.0) about 120 days after the
141 mainshock (Fig. 2b).

142 The seismic-moment (M₀) release during the ZES has not been uniform (Fig. 2c). In
143 addition to the energy released during the mainshock, two M>5 earthquakes that occurred on
144 January 11th, 2014 (M_w 5.1) and on March 29th, 2016 (M_w 5.4) dominate the graph in Figure 2c.
145 A further M_w 4.9 earthquake struck about 30 minutes before the mainshock (22:22 UTC);
146 however, its seismic-moment is poorly resolved (Fig. 2c), as it is overprinted by the
147 mainshock's moment release. The total M₀ released in the ~5 years prior to the mainshock is

148 equivalent to a \sim M5.8 earthquake, while the cumulative M_0 released during the entire ZES is
149 equivalent to a \sim M7 earthquake (Table S1).

150 Seismicity rates within the ZES also vary through time (Fig. 2c). For example, a 6-
151 month interval of increased seismicity (September 2016 to April 2017) is preceded (December
152 2015 to August 2016) and followed (May 2017 to October 2018) by yearlong periods where the
153 seismicity rates are lower, especially proximal to the epicentral area of the M_w 6.9 earthquake
154 (Fig. 2a,c and Fig. S2). This swarm-like activity initiated \sim 1.5 years before the mainshock and
155 is characterised by 3 times higher seismicity rates compared to the preceding and following
156 time-periods, absence of a dominant earthquake at the start of the sequence, spatiotemporally
157 clustered events in the proximity of the (future) mainshock location, and the largest (1.59)
158 coefficient of variation (CV) during the ZES (Fig. 2c,d). These characteristics collectively
159 indicate temporally clustered earthquake activity.

160 To assess whether these fluctuations in the seismicity rates reflect stress changes within
161 the Earth's crust, we have calculated the evolution of the b-value of the Gutenberg-Richter
162 frequency-magnitude distribution in the study area, from January 2013 to May 2019 (Fig. 2d
163 and Fig. S1c). The b-value in a given area describes the relative abundance of small to large-
164 magnitude earthquakes at that location and, thus, any temporal variation in b-values is often
165 interpreted to reflect changes in the confining stress within the seismogenic crust (Schorlemmer
166 et al., 2005). Namely, b-values have been found to relate inversely to differential stresses, with
167 low (<1) b-values often indicating elevated stress while high (>1) b-values indicate
168 low/heterogeneous stresses. Here, b-values were derived for subsets of 500 earthquakes with
169 half-overlapping time-windows for the foreshock sequence (01.01.2013 to 25.10.2018) and for
170 subsets of 1000 events in the aftershock sequence (for more details on the b-value calculation
171 refer to Text S1 in the Supporting Information). We find that during the \sim 70 months preceding
172 the mainshock, b-values in the ZES fluctuate over four main time-intervals (Fig. 2d and Fig.
173 S1c): (i) from January 2013 to December 2014 the b-value is uniform and about 1 (0.94 ± 0.09);
174 (ii) from January 2015 to August 2016, the b-value drops significantly (as low as 0.81); (iii)
175 from September 2016 to April 2017, there is a sharp increase in the b-values (up to 1.36) while
176 (iv) from May 2017 till the mainshock (October 25th, 2018), the b-value drops again below 1
177 (average of 0.88 ± 0.08). The mean b-value of the aftershock sequence is 1.18 ± 0.12 , in
178 agreement with values from other aftershock sequences worldwide (Gulia et al., 2018). In

179 summary, b-values in the ZES remained uniform and equal to ~ 1 during 2013 and 2014, while
180 from early 2015 until the main-shock in late 2018 the b-values were overall < 1 , except for the
181 6-month time-period of the swarm-like activity (Fig. 2d). For a sequence such as the ZES,
182 where multiple faults appear to be active simultaneously in the subsurface (Figs 1-4),
183 earthquake relocation is vital, not only because it allows delineation of individual earthquake
184 clusters with discrete faults (Waldhauser and Ellsworth, 2002) but also because it may help
185 identify day-to-month long earthquake interactions between neighbouring faults
186 (Mouslopoulou and Hristopulos, 2011).

187

188 **3.2 Earthquake relocation**

189 We successfully relocated 12,620 earthquakes that occurred within the ZES from
190 01.01.2014 until 31.05.2019 (Fig. 3), using a local minimum 1-D velocity model (Sachpazi et al.,
191 2000) and manually picked P & S phase onsets determined at the National Observatory of
192 Athens (NOA). The main challenges associated with the relocation arose from the large
193 azimuthal gaps (average $> 180^\circ$) between the seismic source and the seismographs, the poor
194 station density and the complex velocity structure of the study area (Karastathis et al., 2015). We
195 used a constant V_p/V_s ratio of 1.80 in accordance with other seismological studies in the area
196 (Kassaras et al., 2016; Haddad et al., 2020). Pick quality classes and associated errors derive
197 from NOA (Table S2). Our preferred earthquake location software is the Non Linear Location
198 (NLLoc) (Lomax et al., 2000) that uses a non-linear location algorithm which is thought to
199 provide more reliable solutions and hypocentre error estimates in case of ill-conditioned
200 locations (such as those encountered within the ZES). For more details on the earthquake
201 relocation refer to Text S2 in the Supporting Information. Overall, the relocation of the ZES
202 reduced the average RMS from 0.39 (revised NOA catalogue) to 0.2, with average horizontal
203 and vertical errors of ~ 3.8 km (in Hypo71 format from NLLoc).

204 The most intriguing finding from the relocation is that, in the foreshock sequence, the vast
205 majority of the earthquakes ruptured the upper 20 km of the crust through four main clusters (i-iv
206 in Fig. 3a-b), each of which appears to have involved slip on multiple inferred slip surfaces (see
207 red dashed lines in Fig. 3). Our results are broadly consistent with those of Sokos et al. (2020)
208 and Haddad et al. (2020), although these studies focus on subsets of the ZES. Earthquake
209 relocation highlights a prominent gap in the seismicity between Zakynthos and western

210 Peloponnese during the foreshock sequence, at depths ranging from ~7 to 20 km (Fig. 3a-b). This
211 feature persists also, perhaps slightly less pronounced, during the aftershock sequence (Fig. 3c).
212 To better evaluate possible interrelations between these clusters and assess their impact in the
213 ZES evolution, below we constrain the kinematics of these earthquakes.

214

215 **3.3 Earthquake focal mechanisms**

216 We have obtained the moment tensors (MTs) of 102 earthquakes that occurred during the
217 ZES by inverting regional broadband data and fitting full waveform and amplitude spectra in the
218 time and frequency domain (Cesca et al. 2010, 2013; Heimann et al., 2018; Figs S3-S4, see the
219 Text S3-S4 in the Supporting Information for more details). The studied earthquakes range in
220 moment magnitude from M_w 3.9 to M_w 6.9, show shallow crustal depths down to about 25 km,
221 and are associated with all types of faulting, with a predominance of strike-slip and thrust
222 mechanisms (Fig. 5 and Table S4). Seventeen of these events (Figs 3 and 5) have occurred in the
223 time-period that precedes the main earthquake (October 25th, 2018), one is the mainshock and
224 the remaining 84 occurred during the aftershock sequence (Fig. 5).

225 The most interesting result of the MT inversion is that it demonstrates a high variability of
226 MT configurations and faulting style over a quite compact region, extending laterally less than
227 60 km (Figs 1 and 5). Most of the 102 MT solutions could be classified (Cesca, 2020; see Fig.
228 S5) into 8 families, each sharing similar focal mechanisms, spanning from pure strike-slip to
229 pure thrust and normal faulting. The variability in these mechanisms is consistent with a NE-SW
230 trending pressure axes, in agreement with the convergence direction, and a NW-SE tension axis
231 (Fig. 5c). This faulting style complexity is supported by offshore seismic-reflection profiles (e.g.,
232 Kokkalas et al., 2013; Wardell et al., 2014; this study) that indicate abundance of deep-thrust and
233 shallow normal faulting as well as steeply dipping strike-slip faults (Fig. 4). This is also
234 evidenced in the diverse present-day crustal stress field inferred from regional-scale inversion of
235 focal mechanisms (Konstantinou et al., 2017). Further, our data support a clear difference among
236 the distribution and predominance of different focal mechanisms before and after the mainshock
237 (Figs 3 and 5). Results suggest the activation of a complex, shallow (< 20 km) fault network and
238 the presence of strong stress heterogeneities, probably induced or enhanced by the occurrence of
239 the M_w 6.9 event in the ZES, which was able to trigger microseismicity across a range of fault
240 geometries and faulting styles (Fig. 5c). The average depth of reverse faulting, which occur

241 mostly at the western edge of the hypocentral cloud of the main event, is ~10 km, while for
242 strike-slip and normal faulting, which occurs also east of Zakynthos and on Peloponnese, is ~8
243 and 9 km, respectively (Table S4 and Figs. S6-S7).

244

245 **3.4 Foreshock kinematics**

246 In the years preceding the ZES, the focal region is characterized by diffuse seismicity that
247 highlights different local spatial clusters and different styles of faulting (Figs 3a-b, 5a). Most
248 prominent clusters are found at about 37.5°N, 20.6°E, in the vicinity of the 2018 M_w 6.9
249 mainshock and close to the Peloponnese coastline, both onshore and offshore (Figs 3a-b, 5a).
250 The clusters appear to mostly delineate along a NW-SE direction (Fig. 3a-b), marking known
251 active faults both offshore western Peloponnese (Kokkalas et al., 2013; Wardell et al., 2014;
252 Makris and Papoulia, 2014; Haddad et al., 2020) and onshore (Fountoulis et al., 2015), some of
253 which have recently hosted large-magnitude historic earthquakes (e.g., the 1997 M_w 6.5
254 Strofades earthquake; Kiratzi and Louvari, 2003) (Fig. 1). In addition to the NW-SE striking
255 earthquake clusters, a NE-SW cluster in onshore Peloponnese appears to delineate the large
256 NE-SW right-lateral strike-slip Movri Fault that produced the 2008 M 6.4 Movri Earthquake
257 (Fig. 3a-b and Fig. S2a-b) (Konstantinou et al., 2009; Cesca et al. 2010). This fault is active
258 during the ZES foreshock sequence down to depths of ~20 km (Movie S1). Indeed, distinct
259 deep (c. 0-20 km) and shallow (< 5 km) seismicity clusters from June to November 2015 and
260 from May to August 2016, respectively, highlight intermittent activity on sections of the Movri
261 Fault (Movie S1 and Fig. S14). The horizontal (dextral) sense of slip on this fault is further
262 supported by the strike-slip focal mechanisms recorded along this structure prior to the main
263 event (Fig. 5a).

264 Moment tensor analysis (Fig. 5) coupled with earthquake relocation (Fig. 3) suggest that
265 the early phase of the ZES involved slip on a series of steeply dipping NW-SE trending left-
266 lateral strike-slip faults offshore western Peloponnese, at depths ranging from 15 to 20 km (see
267 along-strike distance of 120-130 km on Profile A-A' in Figure 3a). The predominantly sinistral
268 strike-slip faulting is in agreement with focal mechanisms obtained by Haddad et al. (2020). In
269 the following 3.5 years, seismicity migrated first eastward (towards onshore Peloponnese),
270 involving strong interactions between faults immediately offshore and onshore western
271 Peloponnese (Fig. 3a-b) while earthquake activity west of Zakynthos was minimal, and from

272 November 2015 until October 2018, the seismicity of the ZES migrated westward, towards the
273 epicentral area of the M_w 6.9 event (Movie S1). During the entire foreshock sequence (1-1-2014
274 to 25-10-2018), the ZES involved slip on mainly strike-slip and normal faults, with negligible
275 contribution of thrust faulting (Fig. 3a & b, Fig. 5).

276

277 **3.5 Mainshock and aftershock kinematics**

278 The mainshock of the Zakynthos Earthquake is characterized by an oblique (thrust to
279 strike-slip) mechanism. A full moment tensor inversion suggests a significant non-double-couple
280 component (Fig. 6), as proposed also by global catalogues (Global CMT) and previous studies
281 (e.g. Sokos et al. 2020). This MT solution is compatible with the combination of two sources (as
282 proposed also by Sokos et al., 2020), one characterized by thrust faulting, similar to those
283 resolved for a cluster of aftershocks north of the mainshock hypocenter, and one by strike-slip to
284 oblique mechanism, as found for several aftershocks east of the mainshock hypocentre (Fig. 5b
285 and Fig. S6). These two individual sources share a common pressure axis with our overall MT
286 solutions (Fig. 5c and Fig. 6).

287 The aftershock sequence of the Zakynthos Earthquake appears outstanding in its
288 heterogeneities. Seismicity spreads over about 60 km along the trench and 50 km across it (Figs
289 3c and 5b), and involves all type of earthquake types, including strike-slip, normal, thrust and
290 oblique faulting (Fig. 5c), suggesting complex fault patterns on multiple faults of different depths
291 and orientations. This is in agreement with local stress heterogeneities and fault diversity
292 suggested for the study area by Konstantinou et al. (2017). The spatial distribution of the
293 aftershocks presents two main trends: (1) the progressive localisation of aftershocks towards the
294 epicentral area of the main event (Fig. 3c), and (2) long-range (>50 km) interactions between the
295 epicentral region and earthquakes occurring within clusters (i) and (ii) (Fig. 3c). The latter fault
296 interactions initiated ~2 months after the mainshock and are animated in Movie S1.

297 The mainshock and some aftershocks (Fig. 5b) suggest the rupture of an NNE-SSW
298 striking and ESE-dipping ($\sim 50^\circ$) thrust fault, which most likely reflects a thrust fault in the
299 overriding plate (as opposed to the subduction plate-interface) (Figs 3, 5 and 6; Table S4), in
300 agreement with results from Cirella et al., (2020) and Sokos et al., (2020). The latter is supported
301 by published seismic-reflection and bathymetric data (Figs 1 and 4, Fig. S17) that reveal
302 numerous \sim NNW-SSE trending thrusts that dip 30 - 50° to the northeast, beneath Zakynthos and

303 western Peloponnese (Sachpazi et al., 2000; Kokkalas et al., 2013; Wardell et al., 2014; Makris
304 and Papoulia, 2014; this study) and the recording of a minor tsunami (10 cm) along the western
305 coastline of Peloponnese that suggests rupture of the sea-bed (Cirella et al., 2020). It is also
306 supported by the low-dipping (15-17°) angle of the plate-interface beneath the epicentral area
307 (e.g. Halpaap et al., 2018). Nevertheless, the majority of the aftershocks mark the activation of
308 other faults (Fig. 5b). The location, depth and focal mechanisms of the latter events are
309 incompatible with both the mainshock rupture plane and the geometries recorded during the
310 foreshock activity (Figs. 3 and 5). Specifically, joint analysis of the location and mechanisms of
311 the aftershock sequence suggests the activation of multiple steeply-dipping strike-slip faults that
312 run in ~NE-SW orientations (and at high angles to the trench). The seismicity is confined above
313 the subduction interface (<20 km) and deepens accordingly towards the coast of the Peloponnese
314 (Fig. 5e-f). A second family of events (blue in Figs 5b-f) denote normal faulting along one or
315 more additional NW-SE faults. Normal faulting earthquakes mostly occurred at shallow depths,
316 indicating reactivation in the aftershock sequence of shallow normal faults located mostly on the
317 hangingwall of thrust faults (Kokkalas et al., 2013; Wardell et al., 2014; this study) (Fig. 4). It is
318 noteworthy that focal mechanisms between the island of Zakynthos and western Peloponnese
319 (cluster ii in Fig. 3a-b) mark a similar region as in the years preceding the main event, but with
320 different mechanisms (Fig. 5), suggesting that stress perturbations during the mainshock are able
321 to inhibit strike-slip and oblique-normal mechanisms, which were dominant before October 25th
322 2018, and favour strike-slip and extensive pure thrust faulting. Fault slip reversed between the
323 interseismic and postseismic periods has been also observed on crustal faults in Chile and is
324 linked to the megathrust seismic cycle (Shirzaei et al., 2012).

325

326 **4 Slow-slip events during the ZES**

327 To assess the likely involvement of aseismic slip transients in the evolution of the ZES, we
328 analyse the deformation on the Earth's surface recorded by 10 permanent GPS stations located
329 within the broader study area (Fig. 1). We find that the earthquake activity within the ZES was
330 accompanied by aseismic-slip release in the form of two slow slip events (SSEs). Below, we first
331 discuss the analysis and modelling of the GPS data and, following, we present evidence for two
332 prominent GPS transient signals – which are the first SSEs to be recorded in the HSS.

333

334 **4.1 GPS time-series analysis and modelling**

335 Continuous GPS data with daily recordings were obtained from 10 permanent GPS stations
336 located along western Peloponnese and the island of Zakynthos (Fig. 1). We analysed the
337 ITRF08 daily coordinates of 5 stations (TRIP, RLSO, PYRG, PYL1 and PAT0) available at the
338 NEVADA Geodetic Laboratory (<http://geodesy.unr.edu/magnet.php>; Blewitt et al., 2018) and of
339 5 stations (063A, 003A, 028A, 030A, 029A) that belong to the HEPOS network of the Hellenic
340 Cadastre. Collectively, our GPS dataset provides observations for a period of ~5.5 years (from
341 01.01.2014 till 31.05.2019) which is comparable to the time-period of the ZES (Fig. 2e). The
342 recordings at stations PYRG, RLSO and TRIP have, however, slightly shorter duration (see Fig.
343 2d and Supplementary Figs S8-S9). For more details on the geodetic dataset used in this study
344 see Text S5 in the Supporting Information.

345 As a first step in our analysis, we removed outliers from the GPS signal by applying the
346 Hampel filter, a common approach for reducing noise (Pearson, 2005). Subsequently, we applied
347 the Greedy Automatic Signal Decomposition algorithm (GrAtSiD; Bedford and Bevis, 2018) to
348 decompose the GPS signal into (i) the seasonal oscillation signal; (ii) secular and transient
349 motions and (iii) the residual signal. The secular motion corresponds to the long-term velocity of
350 the station, which is in principle stable, while the transient signal is estimated by fitting a
351 minimum number of multi-transient signals that are defined as the sum of two or more
352 exponentially decaying time functions. The modelled signal is derived by using a linear
353 regression representing a trajectory model (see Bevis & Brown, 2014). The onset of the transient
354 signal is not pre-defined, as GrAtSiD automatically detects possible transient onsets. We applied
355 the GrAtSiD time series decomposition using a station-by-station and component-by-component
356 approach (Fig. S8). This process was repeated 250 times in order to retrieve the statistical
357 information (median and interquartile range) of the 250 modelled trends (red lines in Figs S8 and
358 S9) resulting, thus, in a time-dependent estimate of the velocity uncertainty.

359 Transient signals in GPS timeseries may be tectonic (e.g., Wallace and Beavan, 2010) but
360 may also be due to environmental or anthropogenic conditions, such as high precipitation rates or
361 monument instability (Williams et al., 2004; Larson et al., 2008). To account for non-tectonic
362 signal, we assessed the maintenance history of all ten stations used in this analysis as well as the
363 fluid loading history in the area. The latter was predicted at each station location based on the
364 ESMGFZ model (<http://rz-vm115.gfz-potsdam.de:8080/repository>), which produces values of

365 elastic surface loading (Dill and Dobslaw, 2013; doi:10.1002/jgrb.50353). Transient signal in the
366 fluid loading timeseries was modeled using GrAtSiD (Fig. S11 and Movie S2). Results suggest
367 that there is no strong correlation in space and/or time between the two GPS transients and the
368 predicted fluid transients, which are mostly very short-lived (Fig. S11 and Movie S2). Therefore,
369 the recorded transients are very likely tectonic.

370

371 **4.2 Slip transients during the ZES**

372 Tectonic transient signals in a GPS timeseries may be related to SSEs and/or post-seismic
373 relaxation (e.g., Sun et al., 2014). The latter is excluded because there is no large ($M > 6$)
374 earthquake in the foreshock sequence (Bedford et al., 2016). To assess the spatiotemporal
375 changes of the GPS velocity pattern within the study area, we calculate the daily median GPS
376 network velocity along the east component, which is normal to the trench (Fig. 2e). Examination
377 of Figure 2e reveals two significant changes in the GPS velocities both associated with an
378 eastward acceleration of the mean velocity of the vectors before their abrupt westward rotation
379 (Fig. 2e). The first of these transients occurs in late 2014 and lasts slightly more than 6 months,
380 while the second starts in mid-2018 and continues until prior to the M_w 6.9 earthquake, lasting
381 for about 5 months (Fig. 2e, Fig. 7). Here, we need to clarify that although the transient signal
382 lasts for about 6 and 5 months during the 2014 and 2018 episodes, respectively, the slow slip
383 events themselves have shorter duration (112 days in 2014 and 107 days in 2018; see Fig. 2e and
384 Text S5 in the Supp. Information). This is because each transient signal comprises individual
385 deformational periods of different durations that include, successively, landward network
386 acceleration, trenchward network acceleration (i.e. the SSE) and, for the 2018 transient,
387 landward network acceleration until the main M_w 6.9 event (see below for details). The daily
388 evolution of these velocities, and the associated deformational periods within each transient, can
389 be seen in Movie S3 whereas the interrelation between these SSEs and the seismic-moment
390 release is highlighted in Movie S1.

391 The first transient initiates at 24.09.2014 and terminates at 20.03.2015 (that is, a total of
392 178 days) (Fig. 2e and Movie S3). During this episode all ten stations appear, first, to accelerate
393 eastwards for about two months and, subsequently, to deviate from their main equilibrium
394 position and rotate westwards (Figs 2e and 7a & 7c and Movie S3). Maximum cumulative
395 displacement of about 5 mm is recorded at station 028A in Zakynthos, while attenuated

396 displacements are observed in eastern and southern Peloponnese (e.g. stations 030A, 063A and
397 TRIP; Fig. 7). The small vector obliquity observed at station 028A in Zakynthos with respect to
398 vectors in Peloponnese, possibly indicates the involvement in this slow-slip event of additional
399 (mainly strike-slip) structures of offshore Peloponnese (e.g., Bürgmann, 2018). No significant
400 microseismicity is associated with this SSE (Movie S3).

401 The second transient signal spans the time-period between 14.05.2018 and 25.10.2018
402 (~164 days), immediately preceding the M_w 6.9 Zakynthos Earthquake (Fig. 2e). This SSE
403 shows very similar characteristics to those recorded during the 2014-2015 transient (e.g.,
404 acceleration and trenchward rotation of the vectors; see Fig 2e, Fig 7d and Movie S3). Here, the
405 vector acceleration lasts also for ~2 months, followed by a trenchward rotation of the vectors
406 (Fig 2e, Fig 7 and Movie S3) and velocity acceleration until the Zakynthos mainshock (Fig. 7d).
407 Interestingly, here, station 028A at Zakynthos Island records each deformational phase
408 (acceleration/rotation/readjustment and acceleration) with a time delay of ~30 days compared to
409 the remaining stations (see Movie S3). This likely suggests an upward migration of slip from
410 greater depths (beneath Peloponnese) to shallower depths (beneath Zakynthos). Similarly to the
411 2014 SSE, cumulative maximum displacement is observed on Zakynthos (station 028A) and is of
412 comparable size (5.3 mm) to the 2014 transient. This transient is associated with shallow (<10
413 km) seismic-moment release proximal to the epicentral area (Movie S1 and Fig. S15).

414 The widespread occurrence of deformation along the entire western Peloponnese and
415 Zakynthos Island, coupled with the trenchward orientation of the vectors (Fig. 7a-b), collectively
416 suggest that both transients likely originate on the subduction plate-interface that extends beneath
417 central-western Peloponnese. To better explore the origin and spatial distribution of these two
418 transients we performed forward modelling and, assuming a homogeneous elastic half-space and
419 using the analytical equations of Okada (1985), obtained surface displacements by assigning slip
420 on the plate-interface (Fig. S12). After testing for various displacement scenarios we derived, for
421 each SSE, the best uniform-slip model by allowing average slip of 5 mm on the plate-interface
422 (Fig. S12c). The total geodetic moment released during each SSE is 3.20×10^{18} Nm and
423 corresponds to a M_w ~6.3 earthquake (Table S1). The relationship between geodetic moment
424 release / duration of the Zakynthos transients is similar to the relationships observed for other
425 tectonic transient signals globally (Fig. S13; Peng and Gomberg, 2010), reinforcing the tectonic
426 origin of these deformational episodes. Some discrepancies observed in the north of the study

427 area (Fig. S12), likely reflect additional distributed slip on the plate-interface and/or upper-plate
428 faults. Thus, the estimated average slip of 5 mm on the plate-interface should be considered as
429 the minimum slip required for reproducing the observed surface deformation. Slip-inversion of
430 the transient events will allow better assessment of their spatial distribution and is currently in
431 progress (Saltogianni et al. Pers. Com). Further, the acceleration of the vectors observed prior to
432 both slow-slip events was recorded in all 10 stations to last for about 2 months in each case (Fig
433 2e, Fig. 7 and Movie S3). This acceleration may be indicative of deep active processes related to
434 changes in slab pull force (Bedford et al., 2020) and/or to a dynamic increase of locking along
435 the plate-interface zone prior to seismic or aseismic slip events (Materna et al., 2019). The
436 described SSEs of this study are the first to be reported in the HSS.

437

438 **5 The preparatory phase leading to the M6.9 Zakynthos Earthquake**

439 Our data suggest that the b-values in the ZES systematically dropped below 1 soon after
440 the trenchward rotation of the GPS velocity vectors during the 2014-2015 transient (Fig. 2d-e
441 and Supplementary Fig. S1c). Since that time, and until the main event in late 2018, the b-
442 values in the ZES remained overall suppressed (<1), with one exception: the ~6-months
443 (September 2016 to April 2017) where swarm-like microseismicity ruptured repeatedly the
444 epicentral area accounting for high b-values (up to 1.36) and strong spatiotemporal earthquake
445 clustering (Fig. 3b, Supplementary Fig. S2c and Movie S1); note that high b-values were again
446 encountered only in the aftershock sequence ($b \sim 1.2$; Fig. 2d). Suppressed b-values (<1) have
447 been observed prior to mainshocks globally (e.g. Nuannin et al., 2005; Schurr et al. 2014). On
448 the other hand, elevated b-values (>1) often characterise aftershock sequences and/or
449 earthquake swarms (Scholz, 2015; Gulia et al. 2018). The fluctuations recorded in the b-values
450 of the ZES during the ~5 years preceding the mainshock are in accordance with these
451 observations (Fig. 2d), with low b-values (<1) most likely indicating increased stresses in the
452 crust during the years preceding the main event (Schorlemmer et al., 2005).

453 Combining the above, we propose a scenario in which the SSE that occurred beneath
454 western Peloponnese in late 2014, tectonically destabilized ($b < 1$) the western termination of the
455 subduction system to, first, trigger swarm-like activity in the epicentral area of the main-shock
456 in late 2016 and, subsequently, the M_w 6.9 Zakynthos Earthquake (Figs. 2 and 3). As discussed
457 in Section 4.2, it is likely that the first SSE involved, in addition to slip on the plate-interface, a

458 triggered slow-slip on one (or more) strike-slip structures in the upper-plate (see vector
459 obliquity between Zakynthos/mainland in Fig. 7a), a scenario that could promote widespread
460 stress changes in the upper-plate (e.g. Hamling and Wallace, 2015). The persisting low (<1) b -
461 values in the ZES after the first SSE and until the M_w 6.9 Zakynthos Earthquake about 4.5 years
462 later, suggests significant stress perturbations which were not fully accommodated during the
463 swarm seismic-moment release (equivalent to a $\sim M_w$ 4.9; Table S1) in the broader epicentral
464 area of the Zakynthos mainshock. Interestingly, following these swarms, the epicentral area
465 remained mostly quiet for the following year (from May 2017 to April 2018; Movie S1) before
466 it becomes next active with the onset of the second transient in May 2018 (Movie S1 and Fig.
467 S15).

468 The second transient immediately precedes the main M_w 6.9 Zakynthos Earthquake (Fig
469 2d,e and Fig. 7b; Movie S3). The ~ 30 day phase-lag recorded in the reversal of the GPS vectors
470 between Zakynthos (028A) and the rest of western Peloponnese (e.g., 030A, 029A, etc.),
471 suggests the gradual up-dip migration of slip along the plate-interface, from ~ 40 km depth
472 beneath Peloponnese to shallower crustal depths (<20 km) near Zakynthos (Fig. 7d and Movie
473 S3). It is possible for SSEs that operate either on the subduction plate-interface (Wallace and
474 Beavan, 2010) or nearby crustal faults (Hamling and Wallace, 2015; Bürgmann, 2018), to
475 trigger stress changes in the crust that would lead to generation of large-magnitude earthquakes.
476 Whether this up-dip slip migration a few days before the mainshock produced static-stress
477 changes on one or more upper-plate faults (King et al., 1994) capable of triggering the
478 Zakynthos Earthquake, is investigated in a follow-up study (Saltogianni et al. Pers. Com).

479

480 **6 Interplay between seismic and aseismic deformation at the termination of the HSS**

481 Our analysis records successive phases of seismic and aseismic deformation during the
482 build-up to the M_w 6.9 Zakynthos Earthquake. One question that arises is what drives this type of
483 deformation and how representative this may be in accommodating plate-motion over multiple
484 earthquake-cycles. Slow-slip events that trigger swarm activity and/or moderate-to-large-sized
485 earthquakes have been recorded before in major subduction zones globally, including New
486 Zealand, Japan, Ecuador, Chile and Mexico (Beavan et al., 2007; Kato et al., 2012; Vallée et al.,
487 2013; Ruiz et al., 2014; Obara and Kato, 2016; Colella et al., 2017). Although the detailed
488 distribution of interseismic coupling beneath western Peloponnese in Greece has not been

489 constrained, a first-order difference between the global examples and the Greek case is that the
490 SSEs here occur on a weak plate-interface that largely creeps (Vernant et al., 2014; Saltogianni
491 et al., 2020). The only other references for SSEs along creeping sections of the plate-interface (or
492 sections with heterogeneous interseismic coupling) is at the central/northern Hikurangi margin in
493 New Zealand (Wallace et al., 2016), in Ecuador (Vallee et al. 2013), Costa Rica (Davis et al.
494 2015) and the Boso Peninsula in Japan (Ozawa et al. 2007). In all these cases, however, the SSEs
495 occur near the trench, at shallow (<10 km) sections of the plate-interface, and are accompanied
496 by intense earthquake activity. By contrast, the SSEs at Zakynthos are deep (~20-40 km) and
497 mostly seismicity free (Movie S3).

498 One possible explanation for the occurrence of aseismic transients at these depths of the
499 HSS (i.e. 20-40 km) is that they mark the downdip end of locally isolated locked patches (Lay,
500 2015). Such patches have been recently discovered south of Crete (Saltogianni et al., 2020) and
501 between Crete and Peloponnese (Howell et al., 2017), where they locally appear to accumulate
502 interseismic strain that may account for up to 85% of the plate-motion. Seismic tomography
503 coupled with analysis of seismic attributes beneath the area of ZES suggests the existence of a
504 high (~1.9) V_p/V_s ratio zone at crustal depths ranging between ~10-30 km (Halpaap et al.,
505 2018), which is indicative of water-rich fluids (Audet et al., 2009) (Fig. 8). As SSEs require very
506 low effective stress (e.g., near lithostatic pore fluid pressures) and high fluid pressures (e.g., Liu
507 and Rice, 2005; Gao and Wang, 2017), their presence beneath western Peloponnese is not
508 surprising. Further, studies have shown that fluids liberated from the plate-interface during SSEs
509 tend to migrate upwards, into the lower portion of the seismogenic zone (Audet et al., 2009;
510 Nakajima and Uchida, 2018) to trigger widespread microseismicity, often in the form of
511 earthquake swarms. The network of strike-slip faults onshore/offshore western Peloponnese
512 (Figs. 1 and 4) is likely to have acted as conduits for fluid migration and triggering of
513 microseismicity within the ZES (Fig. 8), as it is the case with upper-plate faults elsewhere in the
514 Hellenic forearc (Ruscic et al., 2019).

515 Recurring slow-slip events are common along subduction margins and in some cases (e.g.,
516 Nankai Trough megathrust) they appear to accommodate up to >50% of the total plate-motion
517 (Araki et al., 2017). In Greece, two SSEs and significant microseismicity are recorded over a
518 period of ~5 years to precede a large event (Fig. 2d). A question that arises is what percentage of
519 the plate-motion is accommodated by each process operating at the western-end of the HSS. To

520 address this question we have quantified the contribution of each component of deformation
521 (seismic and aseismic) for the period that precedes the M_w 6.9 event (Table S6; for details refer
522 to Text S6 of Supplementary Information). We find that the aseismic slip-rate (produced
523 collectively by the two SSEs) amounts to ~ 2.1 mm/yr (or $\sim 8\%$ of the plate-motion),
524 accommodating significantly more subduction-related strain compared to that produced by the
525 ZES seismicity (slip-rate ~ 1.3 mm/yr or 5% of the plate-motion) (Table S6). These numbers
526 collectively imply that during the ~ 5 years preceding the Zakynthos Earthquake, at least 15% of
527 the plate-motion was released, $\sim 70\%$ was stored elastically (on upper-plate faults and/or the
528 plate-interface), while the remaining $\sim 15\%$ was accommodated by aseismic creep along the
529 downgoing plate (Table S6). Knowing that the average locking along the Hellenic subduction
530 interface is weak (Vernant et al., 2014; Saltogianni et al., 2020) and that the crust beneath the
531 ZES is broken up by numerous upper-plate faults (Figs 1, 4 and 8), we anticipate that a
532 significant fraction of the 70% interseismic strain was stored on one or more faults in the
533 overriding plate. That was confirmed by the M_w 6.9 Zakynthos Earthquake that followed and
534 ruptured faults in the upper crust (Fig. 8). Further, analysis of the aftershock sequence shows
535 that, during the six months following the mainshock, strain equivalent to $\sim 75\%$ of the plate-
536 motion was accommodated by upper-plate faults (Table S1). Similar kinematics characterise the
537 southern termination of the Hikurangi margin in New Zealand, where about 80% of the plate-
538 motion (Wallace et al., 2012) and seismic-moment release during large-magnitude earthquakes
539 (Mouslopoulou et al., 2019) are accommodated by upper-plate faults. Composite faulting
540 patterns accompanied by alternating styles of deformation may characterise multi-fault
541 subduction-termination zones. Our data support the view that the aseismic and seismic
542 displacements observed within the ZES ~ 5 years prior to the M_w 6.9 Zakynthos Earthquake are
543 probably manifestations of very late interseismic stress conditions (i.e. Schurr et al., 2014).
544 Whether these features characterise the seismogenesis at the western termination of the HSS will
545 be tested as additional data from future well-monitored large-magnitude earthquakes become
546 available.

547

548 **7 Conclusions**

549 We have studied the deformation of the Earth's crust where active subduction zones terminate
550 prior and after the 2018 M_w 6.9 Zakynthos Earthquake. Using earthquake, GPS, seismic-

551 reflection and bathymetric data we find that the mainshock was preceded by a synergy of slow-
552 slip events, earthquake swarms and fault-interactions between the subduction thrust and upper-
553 plate faults that lasted about 5.5 years. This long-lasting preparatory phase initiated due to a
554 plate-interface slow-slip event that released strain equivalent to a $\sim M_w$ 6.3 earthquake,
555 tectonically destabilising the upper 20-40 km of the crust and producing alternating phases of
556 seismic and aseismic deformation between the upper-plate and the plate-interface. Tectonic
557 deformation included intense microseismicity ($M < 4$) on neighbouring faults, earthquake swarms
558 in the epicentral area of the mainshock, another episode of slow-slip immediately preceding the
559 mainshock and, eventually, the large (M_w 6.9) Zakynthos Earthquake. Tectonic instability in the
560 area is evidenced by a prolonged (~ 3.5 years) period of overall suppressed b-values (< 1) and
561 strong earthquake interactions on discrete strike-slip, thrust and normal faults. Composite
562 faulting patterns accompanied by alternating (seismic/aseismic) deformation styles may reflect
563 late interseismic stress conditions prior to large-magnitude earthquakes that rupture subduction-
564 termination zones.

565 **Acknowledgments**

566 We thank the staff of the Institute of Geodynamics of the National Observatory of Athens and all
567 partners of the HUSN (including the University of Patras, the University of Thessaloniki, and the
568 University of Athens), for data archiving/processing. In this analysis we used seismological data
569 from stations pertaining to the following networks: GE, IU, II, G, MN, IV, HT, HP, HA, AC, 4A,
570 X5 (data link : <http://www.gein.noa.gr/en/networks/husn>); seismic data and metadata have been
571 downloaded using the FDSN web services of Orfeus ([https://www.orfeus-](https://www.orfeus-eu.org/data/eida/webservices/dataselect/)
572 [eu.org/data/eida/webservices/dataselect/](https://www.orfeus-eu.org/data/eida/webservices/dataselect/)), INGV (<https://doi.org/10.13127/SD/X0FXNH7QFY>),
573 NOA (<https://doi.org/10.7914/SN/HL>), IRIS (<https://service.iris.edu/fdsnws/>) and Geofon
574 (<https://doi.org/10.14470/TR560404>). We are also grateful to the Greek Cadastre (063A, 003A,
575 028A, 030A, 029A) and NEVADA Geodetic Laboratory (i.e., TRIP, RLSO, PYRG, PYL1 and
576 PAT0) for providing the GPS timeseries of the corresponding permanent stations. Many thanks
577 to Dr Dirk Becker for useful discussion on the b-value calculation and to Dr John Begg for help
578 with the block-diagram drawing in Figure 7.

579 **References**

580

- 581 Aki, K. (1966). Generation and Propagation of G Waves from the Niigata Earthquake of June 16,
582 1964: Part 2. Estimation of earthquake moment, released energy, and stress-strain drop
583 from the G wave spectrum. *Bulletin of the Earthquake Research Institute, University of*
584 *Tokyo*, 44, 73-88.
- 585 Albuquerque Seismological Laboratory (ASL)/USGS (1988). Global Seismograph Network -
586 IRIS/USGS. International Federation of Digital Seismograph Networks. Dataset/Seismic
587 Network. 10.7914/SN/IU.
- 588 Anderson, H., & Jackson, J. (1987). Active tectonics of the Adriatic region. *Geophysical Journal*
589 *of the Royal Astronomical Society*, 91, 937-983.
- 590 Araki, E., Saffer, D., Kopf, A., Wallace, L., Kimura, T., Machida, Y., Ide, S., Davis, E., & IODP
591 Expedition 365 Shipboard Scientists (2017). Recurring and triggered slow-slip events
592 near the trench at the Nankai Trough subduction megathrust. *Science*, 356, 1,157–1,160,
593 <https://doi.org/10.1126/science.aan3120>.
- 594 Audet, P., Bostock, M.G., Christensen, N.I., & Peacock, S.M. (2009). Seismic evidence for
595 overpressured subducted oceanic crust and megathrust fault sealing. *Nature*, 457, 76–78.
596 <http://dx.doi.org/10.1038/nature07650>.
- 597 AUTH (Aristotle University of Thessaloniki) (1981). Aristotle University of Thessaloniki
598 Seismological Network. International Federation of Digital Seismograph Networks.
599 10.7914/SN/HT, <https://doi.org/10.7914/SN/HT>.
- 600 Beavan, J., Wallace, L., Douglas, A., & Fletcher, H. (2007). Slow slip events on the Hikurangi
601 subduction interface, New Zealand, in *Dynamic Planet: Monitoring and Understanding a*
602 *Dynamic Planet With Geodetic and Oceanographic Tools: IAG Symposium*, Cairns,
603 Australia, 22–26 August, 2005, Int. Assoc. Geod. Symp., 130, edited by P. Tregoning and
604 C. Rizos, 438–444, Springer, Berlin.
- 605 Bedford, J., Moreno, M., Li, S., Oncken, O., Baez, J.C., Bevis, M., Heidbach, O. & Lange, D.
606 (2016). Separating rapid relocking, afterslip, and viscoelastic relaxation: An application
607 of the postseismic straightening method to the Maule 2010 cGPS. *Journal of Geophysical*
608 *Research*, 121, 7618—7638.

- 609 Bedford, J., & Bevis, M. (2018). Greedy automatic signal decomposition and its application to
610 daily GPS time series. *Journal of Geophysical Research*, 123, B014765, 6992–7003.
- 611 Bedford, J., Moreno, M., Deng, Z., Oncken, O., Schurr, B., John, T., Báez, J.C., & Bevis, M.
612 (2020). Months-long thousand-km-scale wobbling before great subduction earthquakes,
613 *Nature*, 580, 628-635.
- 614 Bevis, M., & Brown, A. (2014). Trajectory models and reference frames for crustal motion
615 geodesy. *Journal of Geodesy*, 88, 283-311.
- 616 Blewitt, G., Hammond, W.C., & Kreemer, C. (2018). Harnessing the GPS data explosion for
617 interdisciplinary science. *Eos* 99, <https://doi.org/10.1029/2018EO104623>.
- 618 Bouchon, M., Durand, V., Marsan, D., Karabulut, H., & Schmittbuhl, J. (2013). The long
619 precursory phase of most large interplate earthquakes. *Nature Geoscience*, 6, 299–302,
620 [doi:10.1038/ngeo1770](https://doi.org/10.1038/ngeo1770).
- 621 Bürgmann R. (2018). The geophysics, geology, and mechanics of slow fault slip. *Earth and*
622 *Planetary Science Letters*, 495, 112–34.
- 623 Cesca, S., Heimann, S., Stammer, K., & Dahm, T. (2010). Automated procedure for point and
624 kinematic source inversion at regional distances. *Journal of Geophysical Research*, 115,
625 [doi:10.1029/2009JB006450](https://doi.org/10.1029/2009JB006450)
- 626 Cesca, S., Rohr, A., & Dahm, T. (2013). Discrimination of induced seismicity by full moment
627 tensor inversion and decomposition. *Journal of Seismology*, 17, 1, 147-163,
628 [doi:10.1007/s10950-012-9305-8](https://doi.org/10.1007/s10950-012-9305-8).
- 629 Cesca, S., Zhang, Y., Mouslopoulou, V., Wang, R., Saul, J., Savage, M., & et al. (2017).
630 Complex rupture process of the Mw 7.8, 2016, Kaikoura earthquake, New Zealand, and
631 its aftershock sequence. *Earth and Planetary Science Letters*, 478, 110-120.
- 632 Cesca, S. (2020). Seiscloud, a tool for density-based seismicity clustering and visualization.
633 *Journal of Seismology*, <https://doi.org/10.1007/s10950-020-09921-8>
- 634 Cirella, A., Romano, F., Avallone, A., Piatanesi, A., Briole, P., Ganas, A. & et al. (2020). The
635 2018 M w 6.8 Zakynthos (Ionian Sea, Greece) earthquake: seismic source and local
636 tsunami characterization. *Geophysical Journal International*, 221, 1043-1054.

- 637 Clément, C., Hirn, A., Charvis, P., Sachpazi, M., & Marnelis, F. (2000). Seismic structure and
638 the active Hellenic subduction in the Ionian islands. *Tectonophysics*, 329, 141–156.
- 639 Colella, H.V., Sit, S.M., Brudzinski, M.R., Graham, S.E., Demets, C., Holtkamp, S.G., & et al.
640 (2017). Seismicity rate increases associated with slow slip episodes prior to the 2012 Mw
641 7.4 Ometepec earthquake. *Earth and Planetary Science Letters*, 464, 35–45.
- 642 Davis, E.E., Villinger, H., & Sun T. (2015). Slow and delayed deformation and uplift of the
643 outermost subduction prism following ETS and seismogenic slip events beneath Nicoya
644 Peninsula, Costa Rica. *Earth and Planetary Science Letters*, 410, 117–27.
- 645 Dziewonski, A.M., Chou, T.-A., & Woodhouse, J.H. (1981). Determination of earthquake source
646 parameters from waveform data for studies of global and regional seismicity. *Journal of*
647 *Geophysical Research*, 86, 2825-2852, doi:10.1029/JB086iB04p02825
- 648 Ekström, G., Nettles, M., & Dziewonski, A.M. (2012). The global CMT project 2004-2010:
649 Centroid-moment tensors for 13,017 earthquakes. *Physics of the Earth Planetary*
650 *Interior*, 200-201, 1-9, doi:10.1016/j.pepi.2012.04.002.
- 651 Fountoulis, I., Vassilakis, E., Mavroulis, S., Alexopoulos, J., Dilalos, S., & Erkeki, A. (2015).
652 Synergy of tectonic geomorphology, applied geophysics and remote sensing techniques
653 reveal the existence of active tectonism in NW Peloponnese (Greece). *Geomorphology*,
654 237, 52-64.
- 655 Gao, X., & Wang, K. (2017). Rheological separation of the megathrust seismogenic zone and
656 episodic tremor and slip. *Nature*, 543, 416-419.
- 657 GEOFON Data Centre, 1993. *GEOFON Seismic Network*. Deutsches GeoForschungsZentrum
658 GFZ. <https://doi.org/10.14470/TR560404>
- 659 Grigoli, F., Cesca, S., Rinaldi, A.P., Manconi, A., Lopez Comino, J.A., Clinton, J.F., et al.
660 (2018). The November 2017 Mw 5.5 Pohang earthquake: A possible case of induced
661 seismicity in South Korea, *Science*, 360, 6392, 1003-1006, doi:10.1126/science.aat2010.
- 662 Gulia, L., Rinaldi, A. P., Tormann, T., Vannucci, G., Enescu, B., & Wiemer, S. (2018). The
663 effect of a mainshock on the size distribution of the aftershocks. *Geophysical Research*
664 *Letters*, 45, 13-277.

- 665 Haddad, A., Ganas, A., Kassaras, I., & Lupi, M. (2020). Seismicity and geodynamics of western
666 Peloponnese and central Ionian Islands: insights from a local seismic deployment,
667 *Tectonophysics*, <https://doi.org/10.1016/j.tecto.2020.228353>.
- 668 Halpaap, F., Rondenay, S., & Ottemöller, L. (2018). Seismicity, Deformation, and
669 Metamorphism in the Western Hellenic Subduction Zone: New Constraints From
670 Tomography. *Journal of Geophysical Research*, 123, 3000-3026.
- 671 Halpaap, F., Rondenay, S., Perrin, A., Goes, S., Ottemöller, L., Austrheim, H.O., & et al. (2019).
672 Earthquakes track subduction fluids from slab source to mantle wedge sink. *Science*
673 *Advances*, 5, doi: 10.1126/sciadv.aav7369.
- 674 Hamling, I.J., & Wallace, L.M. (2015). Silent triggering: aseismic crustal faulting induced by a
675 subduction slow slip event. *Earth and Planetary Science Letters*, 421, 13-19; doi:
676 10.1016/j.epsl.2015.03.046
- 677 Hanks, T.C. & Kanamori, H. (1979). A moment magnitude scale. *Journal of Geophysical*
678 *Research*, 84, 2348-2350.
- 679 Heimann, S., Isken, M., Kühn, D., Sudhaus, H., Steinberg, A., Vasyura-Bathke, H., & et al.
680 (2018). Grond - A probabilistic earthquake source inversion framework. V. 1.0. GFZ
681 Data Services. <https://doi.org/10.5880/GFZ.2.1.2018.003>
- 682 Howell, A., Palamartchouk, K., Papanikolaou, X., Paradissis, D., Raptakis, C., Copley, A., & et
683 al. (2017). The 2008 Methoni earthquake sequence: the relationship between the
684 earthquake cycle on the subduction interface and coastal uplift in SW Greece. *Geophysical*
685 *Journal International*, 208(3), 1592–1610, doi: 10.1093/gji/ggw462
- 686 INGV Seismological Data Centre (2006). *Rete Sismica Nazionale (RSN)*. Istituto Nazionale di
687 Geofisica e Vulcanologia (INGV), Italy. <https://doi.org/10.13127/SD/X0FXNH7QFY>
- 688 INGV (Istituto Nazionale di Geofisica e Vulcanologia) (2009). Emersito Seismic Network for
689 Site Effect Studies in L'Aquila town (Central Italy). International Federation of Digital
690 Seismograph Networks. Dataset/Seismic Network. 10.7914/SN/4A_2009
- 691 Institute of Geosciences, Energy, Water and Environment (2002). Albanian Seismological
692 Network. International Federation of Digital Seismograph Networks. Dataset/Seismic
693 Network. 10.7914/SN/AC

- 694 Institut De Physique Du Globe De Paris (IPGP), & Ecole Et Observatoire Des Sciences De La
695 Terre De Strasbourg (EOST) (1982). *GEOSCOPE, French Global Network of broad*
696 *band seismic stations*. Institut de Physique du Globe de Paris (IPGP).
697 <https://doi.org/10.18715/GEOSCOPE.G>
- 698 Karastathis, V.K., Mouzakiotis, E., Ganas, A., & Papadopoulos, G.A. (2015). High-precision
699 relocation of seismic sequences above a dipping Moho: the case of the January-February
700 2014 seismic sequence on Cephalonia island (Greece). *Solid Earth*, 6, 173-184.
- 701 Kassaras, I., Kapetanidis, V., & Karakonstantis, A. (2016). On the spatial distribution of
702 seismicity and the 3D tectonic stress field in western Greece. *Physics and Chemistry of*
703 *the Earth*, 95, 50-72.
- 704 Kato, A., Obara, K., Igarashi, T., Tsuruako, H., Nakagawa, S., & Hirata N. (2012). Propagation
705 of slow slip leading up to the 2011 Mw 9.0 Tohoku-Oki earthquake. *Science*, 335, 705–
706 708.
- 707 King, G.C., Stein, R.S., & Lin, J. (1994). *Static stress changes and the triggering of earthquakes*.
708 *Bulletin of the Seismological Society of America*, 84, 935–953.
- 709 Kiratzi, A., & Louvari, E. (2003). Focal mechanisms of shallow earthquakes in the Aegean Sea
710 and the surrounding lands determined by waveform modelling: a new database. *Journal*
711 *of Geodynamics*, 36, 251-274.
- 712 Kokinou, E., Kamberis, E., Vafidis, A., Monopolis, D., Ananiadis, G., & Zelilidis, A. (2005).
713 Deep seismic reflection data from offshore western Greece: A new crustal model for the
714 Ionian Sea. *Journal of Petroleum Geology*, 28, 185-202.
- 715 Konstantinou, K. I., Melis, N.S., Lee, S.J., Evangelidis, C.P., & Boukouras, K. (2009). Rupture
716 process and aftershocks relocation of the 8 June 2008 Mw 6.4 earthquake in northwest
717 Peloponnese, western Greece. *Bulletin of the Seismological Society of America*, 99, 3374–
718 3389, doi: [10.1785/0120080301](https://doi.org/10.1785/0120080301).
- 719 Konstantinou, K. I., Mouslopoulou, V., Liang, W.-T., Heidbach, O., Oncken, O., & Suppe, J.
720 (2017). Present-day crustal stress field in Greece inferred from regional-scale damped
721 inversion of earthquake focal mechanisms. *Journal of Geophysical Research*, 122, 506–
722 523. <https://doi.org/10.1002/2016JB013272>.

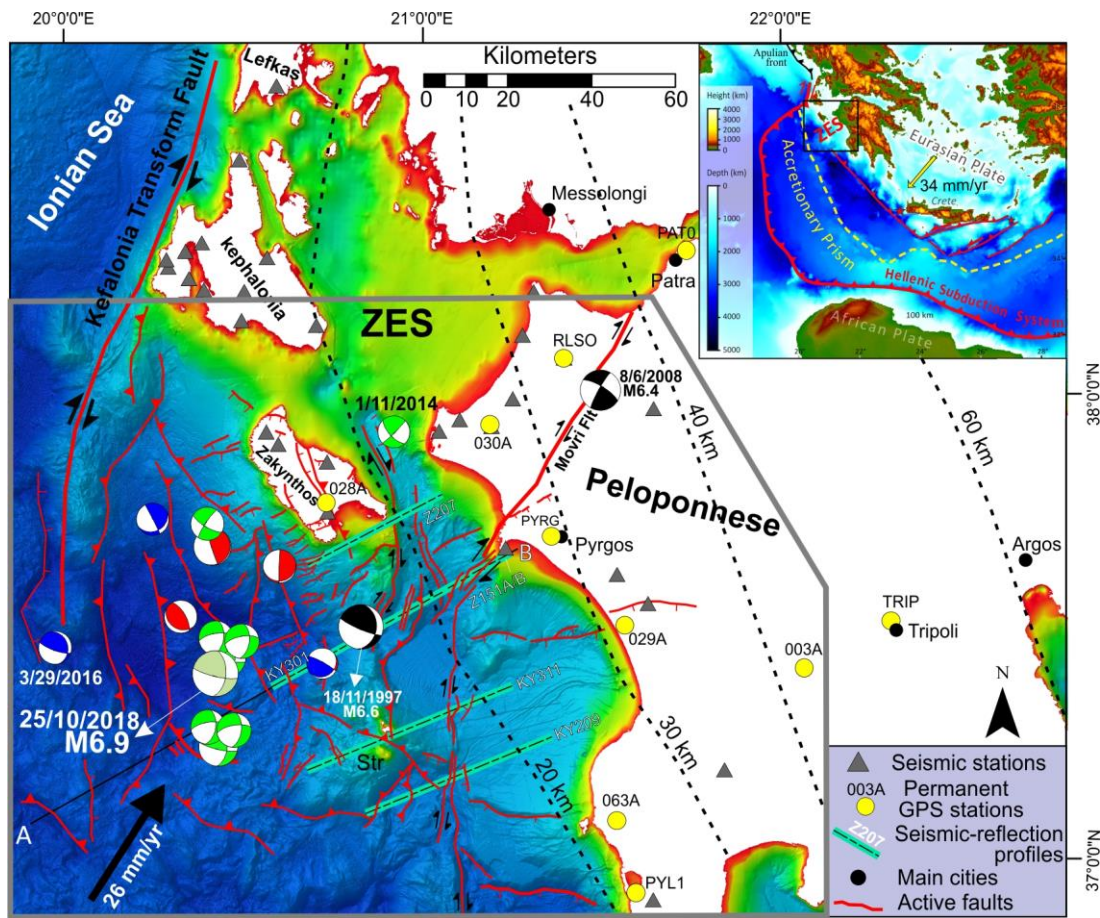
- 723 Larson, K.M., Small, E.E., Gutmann, E.D., & Bilich, A.L. (2008). Use of GPS receivers as a soil
724 moisture network for water cycle studies. *Geophysical Research Letters*, 35, 851–854.
- 725 Lay, T. (2015). The surge of great earthquakes from 2004 to 2014, *Earth and Planetary Science*
726 *Letters*, 409, 133–146.
- 727 Liu, Y., & Rice, J.R. (2005). Aseismic slip transients emerge spontaneously in three dimensional
728 rate and state modeling of subduction earthquake sequences. *Journal of Geophysical*
729 *Research*, 110, B08307, doi:10.1029/2004JB003424.
- 730 Lomax, A., Virieux, J., Volant, P., & Berge-Thierry, C. (2000). Probabilistic earthquake location
731 in 3D and layered models, in: Thurber, C.H., Rabinowitz, N. (Eds.), *Advances in Seismic*
732 *Event Location*, Springer, Dordrecht, Kluwer, Amsterdam, pp. 101–134.
- 733 Lomax, A., Michelini, A., & Curtis, A. (2009). Earthquake Location, Direct, Global-Search
734 Methods, in: Meyers, R.A. (Ed.), *Encyclopedia of Complexity and Systems Science*.
735 Springer New York, New York, NY, pp. 2449–2473.
- 736 Makris J, & Papoulia J., (2014). The backstop between the Mediterranean Ridge and western
737 Peloponnese, Greece: its crust and tectonization. An active seismic experiment with
738 ocean bottom seismographs. *Bollettino di Geofisica Teorica e Applicata*, 55, 249–279.
739 <https://doi.org/10.4430/bgta0125>
- 740 Mann, P., & Frohlich, C. (1999). Classification and tectonic comparison of subduction to strike-
741 slip transitions on active plate boundaries. In: Penrose Conference on Subduction to
742 Strike-Slip Transitions on Plate Boundaries. *Geological Society of America*, Puerto Plata,
743 Dominican Republic.
- 744 McClusky, S., Balassanian, S., Barka, A., Demir, C., Ergintav, S., Georgiev, I., et al. (2000).
745 Global Positioning System constraints on plate kinematics and dynamics in the eastern
746 Mediterranean and Caucasus. *Journal of Geophysical Research*, 105(B3), 5695–5719.
747 <https://doi.org/10.1029/1999JB900351>
- 748 MedNet Project Partner Institutions (1990). *Mediterranean Very Broadband Seismographic*
749 *Network (MedNet)*. Istituto Nazionale di Geofisica e Vulcanologia (INGV).
750 <https://doi.org/10.13127/SD/FBBBTDTD6Q>

- 751 Mouslopoulou, V., Saltogianni, V., Nicol, A., Oncken, O., Begg, J., Babeyko, A., & et al.
752 (2019). Breaking a subduction-termination from top-to-bottom: the 2016 Kaikōura
753 earthquake, New Zealand. *Earth and Planetary Science Letters*, 506, 221-230,
754 <https://doi.org/10.1016/j.epsl.2018.10.020>.
- 755 Mouslopoulou, V., & Hristopulos, D.T. (2011). Patterns of tectonic fault interactions captured
756 through variogram analyses of microearthquakes. *Journal of Geophysical Research*, 116,
757 B07305, <https://agupubs.onlinelibrary.wiley.com/doi/pdf/10.1029/2010JB007804>
- 758 Nakajima, J., & Uchida, N. (2018). Repeated drainage from megathrusts during episodic slow
759 slip. *Nature Geoscience*, 11, 351-356
- 760 Negi, S. S., Paul, A., Cesca, S., Kamal, Kriegerowski, M., Mahesh, P., & Gupta, S. (2017).
761 Crustal velocity structure and earthquake processes of Garhwal-Kumaun Himalaya:
762 Constraints from regional waveform inversion and array beam modeling. *Tectonophysics*,
763 712, 45-63, doi:10.1016/j.tecto.2017.05.007
- 764 NOA (National Observatory of Athens), Institute of Geodynamics, Athens (1997). National
765 Observatory of Athens Seismic Network. International Federation of Digital Seismograph
766 Networks. Dataset/Seismic Network. 10.7914/SN/HL, <https://doi.org/10.7914/SN/HL>.
- 767 Nuannin P., Kulhánek, O., & Persson, L. (2005). Spatial and temporal b-value anomalies
768 preceding the devastating off coast of NW Sumatra earthquake of December 26, 2004,
769 *Geophysical Research Letters*, 32, L11307, doi: 0.1029/2005GL022679.
- 770 Obara, K., & Kato, A. (2016). Connecting slow earthquakes to huge earthquakes. *Science*, 353,
771 253-257.
- 772 Okada, Y. (1985). Surface deformation due shear and tensile faults in a half-space. *Bulletin of*
773 *the Seismological Society of America*, 75, 1135–1154.
- 774 Papazachos, B., & Papazachou, C. (2003). The Earthquakes of Greece. Ziti Publication (In
775 Greek).
- 776 Pearce, D., Rondenay, S., Sachpazi, M., Charalampakis, M., & Royden, L.H. (2012). Seismic
777 investigation of the transition from continental to oceanic subduction along the western
778 Hellenic subduction Zone. *Journal of Geophysical Research*, 117, 1–18.
779 <https://doi.org/10.1029/2011JB009023>

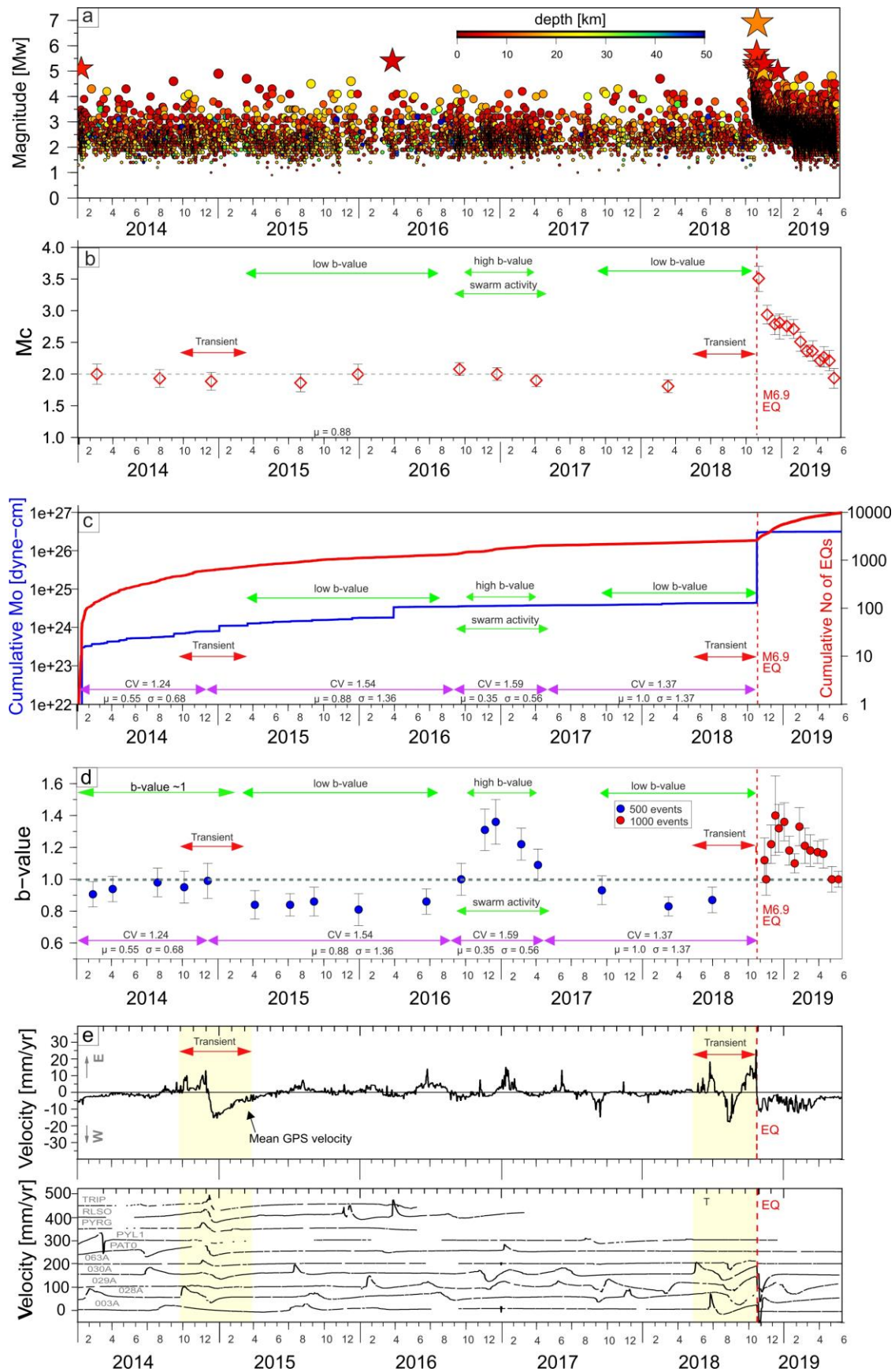
- 780 Pearson K.R. (2005). Mining Imperfect Data: Dealing with Contamination and Incomplete
781 Records, SIAM, 312 pp.
- 782 Pérouse, E., Sébrier, M., Braucher, R., Chamot-Rooke, N., Bourlès, D., Briole, P., & et al.
783 (2017). Transition from collision to subduction in Western Greece: the Katouna–Stamna
784 active fault system and regional kinematics. *International Journal of Earth Sciences*, 106,
785 967–989, doi:10.1007/s00531-016-1345-9.
- 786 Royden, L.H. & Papanikolaou, D.J. (2011). Slab segmentation and late Cenozoic disruption of
787 the Hellenic arc. *Geochemistry, Geophysics, Geosystems*, 12,
788 doi.org/10.1029/2010GC003280.
- 789 Ruiz, S., Metois, M., Fuenzalida, A., Ruiz, J., Leyton, F., Grandin, R., & et al. (2014). Intense
790 foreshocks and a slow slip event preceded the 2014 Iquique M_w 8.1 earthquake. *Science*,
791 345, 165–1169. <http://dx.doi.org/10.1126/science1256074>.
- 792 Ruscic, M., Bocchini, G. M., Becker, D., Meier, T., van Keken, P.E. (2019). Variable spatio-
793 temporal clustering of microseismicity in the Hellenic Subduction Zone as possible
794 indicator for fluid migration. *Lithos*, 346, 105154.
- 795 Sachpazi, M., Hirn, A., Clément, C., Haslinger, F., Laigle, M., Kissling, E., & et al. (2000).
796 Western Hellenic subduction and Cephalonia Transform: Local earthquakes and plate
797 transport and strain. *Tectonophysics*, 319, 301–319.
- 798 Saltogianni, V., Mouslopoulou, V., Oncken, O., Nicol, A., Gianniou, M., & Mertikas, S. (2020).
799 Elastic fault interactions and earthquake-rupture along the southern Hellenic subduction
800 plate-interface zone in Greece. *Geophysical Research Letters*, doi: [10.1029/2019GL086604](https://doi.org/10.1029/2019GL086604).
- 801 Scholz, C.H. (2015). On the stress dependence of the earthquake b value. *Geophysical Research*
802 *Letters*, 42, 1399–1402.
- 803 Schurr, B., Asch, G., Hainzl, S., Bedford, J., Hoechner, A., Palo, M., & et al. (2014). Gradual
804 unlocking of plate boundary controlled initiation of the 2014 Iquique
805 earthquake. *Nature*, 512, 299-302.
- 806 Scripps Institution of Oceanography (1986). Global Seismograph Network - IRIS/IDA.
807 International Federation of Digital Seismograph Networks. Dataset/Seismic Network.
808 10.7914/SN/II

- 809 Shirzaei, M., Burgmann, R., Oncken, O., Walter, T.R., Victor, P., & Ewiak, O. (2012). Response
810 of forearc crustal faults to the megathrust earthquake cycle: InSAR evidence from
811 Mejillones Peninsula, Northern Chile. *Earth and Planetary Science Letters*, 333-334,
812 157-164.
- 813 Sokos, E., Gallovič, F., Evangelidis, C.P., Serpetsidaki, A., Plicka, V., Kostelecký, J., & et al
814 (2020). The 2018 Mw 6.8 Zakynthos, Greece, Earthquake: Dominant Strike-Slip Faulting
815 near Subducting Slab. *Seismological Research Letters*, 91, 721–732, doi:
816 [10.1785/0220190169](https://doi.org/10.1785/0220190169).
- 817 Sokos, E. (2015). Lefkada temporary network. International Federation of Digital Seismograph
818 Networks. Dataset/Seismic Network. 10.7914/SN/X5_2015
- 819 Storchak, D.A., Di Giacomo, D., Bondár, I., Engdahl, E.R., Harris, J., Lee, W.H., & et al. (2013).
820 Public release of the ISC–GEM global instrumental earthquake catalogue (1900–
821 2009). *Seismological Research Letters*, 84, 810-815.
- 822 Sun, T. et al., 2014. Prevalence of viscoelastic relaxation after the 2011 Tohoku-oki earthquake.
823 *Nature* 514, 84–87.
- 824 UA (University of Athens), (2008). Hellenic Seismological Network, University of Athens,
825 Seismological Laboratory. International Federation of Digital Seismograph Networks.
826 Dataset/Seismic Network. 10.7914/SN/HA
- 827 Uchida, N., Iinuma, T., Nadeau, R. M. Bürgmann, R. & Hino, R. (2016). Periodic slow slip
828 triggers megathrust zone earthquakes in northeastern Japan. *Science*, 351, 488–492.
- 829 UP (University of Patras), 2000. University of Patras, Seismological Laboratory. International
830 Federation of Digital Seismograph Networks. Dataset/Seismic Network. 10.7914/SN/HP
- 831 Utsu T. (1965). A method for determining the value of b in a formula $329 \log n = a - bM$
832 showing the magnitude-frequency relation for 330 earthquakes. *Geophysical Bulletin,*
833 *Hokkaido University*, 13, 99–103.
- 834 Vallee, M., Nocquet, J.M., Battaglia, J., Font, Y., Segovia, M., Régnier, M., & et al. (2013).
835 Intense interface seismicity triggered by a shallow slow slip event in the Central Ecuador
836 subduction zone. *Journal of Geophysical Research*, 118, 2965–81.

- 837 Vernant, P., Reilinger, R., & McClusky, S. (2014). Geodetic evidence for low coupling on the
838 Hellenic subduction plate interface. *Earth and Planetary Science Letters*, 385, 122–129.
839 <https://doi.org/10.1016/j.epsl.2013.10.018>
- 840 Wallace, L.M., & Beavan, J. (2010). Diverse slow slip behavior at the Hikurangi subduction
841 margin, New Zealand. *Journal of Geophysical Research*, 115, B12402.
842 <http://dx.doi.org/10.1029/2010JB007717>.
- 843 Wallace, L.M., Barnes, P., Beavan, J., Van Dissen, R., Litchfield, N., Mountjoy, J., & et al. (2012).
844 The kinematics of a transition from subduction to strike-slip: an example from the central
845 New Zealand plate-boundary. *Journal of Geophysical Research*, 117, B02405.
- 846 Wallace, L.M., Webb, S.C., Ito, Y., Mochizuki, K., Hino, R., et al. (2016). Slow slip near the
847 trench at the Hikurangi subduction zone. *Science*, 352, 701–4.
- 848 Waldhauser, F., & Ellsworth, W.L. (2002). Fault structure and mechanics of the Hayward Fault,
849 California, from double-difference earthquake locations. *Journal of Geophysical
850 Research*, DOI: [10.1029/2000JB000084](https://doi.org/10.1029/2000JB000084)
- 851 Wardell, N., Camera, L., Mascle, J., Nicolich, R., Marchi, M., & Barison, E. (2014). The
852 structural framework of the Peloponnese continental margin from Zakynthos to Pylos
853 from seismic reflection and morpho-bathymetric data. *Bollettino di Geofisica Teorica e
854 Applicata*, 55, 343-367.
- 855 Wiemer, S., & Wyss, M. (2000). Minimum magnitude of completeness in earthquake catalogs:
856 Examples from Alaska, the Western United States, and Japan. *Bulletin of the
857 Seismological Society of America*, 90, 859–869.
- 858 Williams, S.D.P., Bock, Y., Fang, P., Jamason, P., Nikolaidis, R.M., Prawirodirdjo, L. et al.,
859 (2004). Error analysis of continuous GPS position time series. *Journal of Geophysical
860 Research*, 109, 1–19.



861 **Figure 1. Overview of the kinematics of the study area and the datasets used.** Map
 862 illustrating the major active faults in the offshore study area and the focal mechanisms of all 14
 863 $M_w > 5$ earthquakes that occurred during the Zakynthos Earthquake Sequence (ZES), including
 864 the M_w 6.9 main event on October 25th 2018, colour coded according to fault style (green=strike-
 865 slip, blue=normal, red=thrust). Two of these events (indicated) occurred prior to the main-shock.
 866 The black moment tensor solutions indicate the epicentres (ISC-GEM; Storchak et al., 2013) and
 867 mechanisms (Global GMT; Dziewonski et al., 1981; Ekström et al., 2012) of the two $M > 6$
 868 earthquakes that occurred in the study area during the instrumental period: the 2008 $M6.4$ Movri
 869 Earthquake onshore Peloponnese and the 1997 $M6.6$ Strofades Earthquake. Grey triangles
 870 indicate the seismic stations used for earthquake-relocation and calculation of moment tensor
 871 solutions, while yellow-circles localities of permanent GPS stations. Lines Z207, KY301-
 872 Z151AB, KY311 and KY209 indicate the localities of the seismic-reflection profiles from
 873 Wardell et al., 2014 (re-interpreted in Figure 4). The bathymetric profile A-B is presented in
 874 Supplementary Fig. S17. Main cities are indicated by black circles. Contours mark the top of the
 875 plate-interface (Halpaap et al., 2019). Offshore bathymetry derived from EMODnet
 876 (<https://portal.emodnet-bathymetry.eu/?menu=19>). Black arrow indicates the relative Eurasia-
 877 Africa plate motion (Pérouse et al., 2017). Inset: the study area is located at the western
 878 termination of the Hellenic subduction margin, the main tectonic features of which are indicated
 879 by red lines. The northward extent of the accretionary prism is indicated by yellow-dashed line.
 880 Bathymetry is from GEBCO. Stars indicate the epicentres of the 365AD (west) and 1303AD
 881 (east) earthquakes in offshore Crete. Yellow arrow indicates the relative Eurasia-Africa plate
 882 motion as derived from GPS measurements (Saltogianni et al., 2020). Str=Strofades islets.



884 **Figure 2 (previous page). Main characteristics of the seismic and GPS deformation**
885 **recorded during the ZES. a,** Moment magnitude (M_w) evolution during the Zakynthos
886 Earthquake Sequence (ZES). Stars indicate events $M > 5$. **b,** Evolution of magnitude of
887 completeness (M_c) through time. **c,** Cumulative seismic-moment and cumulative number of
888 earthquakes during the ZES as a function of time (Jan 1st, 2014 till May 31st 2019). **d,** b-value
889 evolution (and its standard deviation) through time. High and low b-values, slow-slip events and
890 earthquake swarms are indicated on all graphs for comparison. The coefficient of variation (CV)
891 for each time interval is annotated. The average inter-event time (days) and the standard
892 deviation are indicated with μ and σ , respectively. **e,** Evolution of the east GPS component
893 during the ZES, averaged over the stations indicated in the lower panel. Trenchward motion is
894 west. The duration of the two transients observed in the ZES is indicated by red arrows.

895

896

897

898

899

900

901

902

903

904

905

906

907

908

909

910

911

912

913

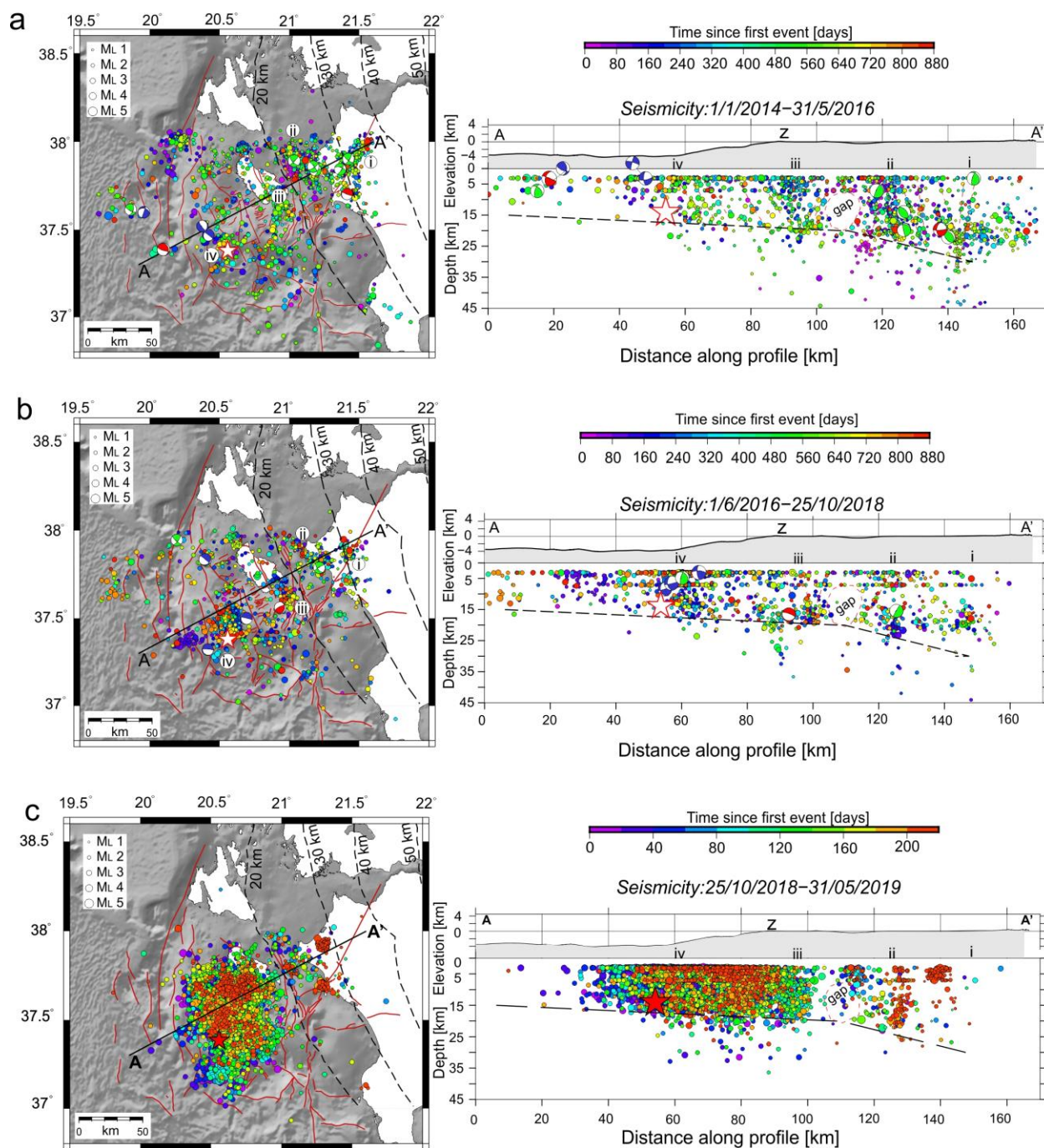
914

915

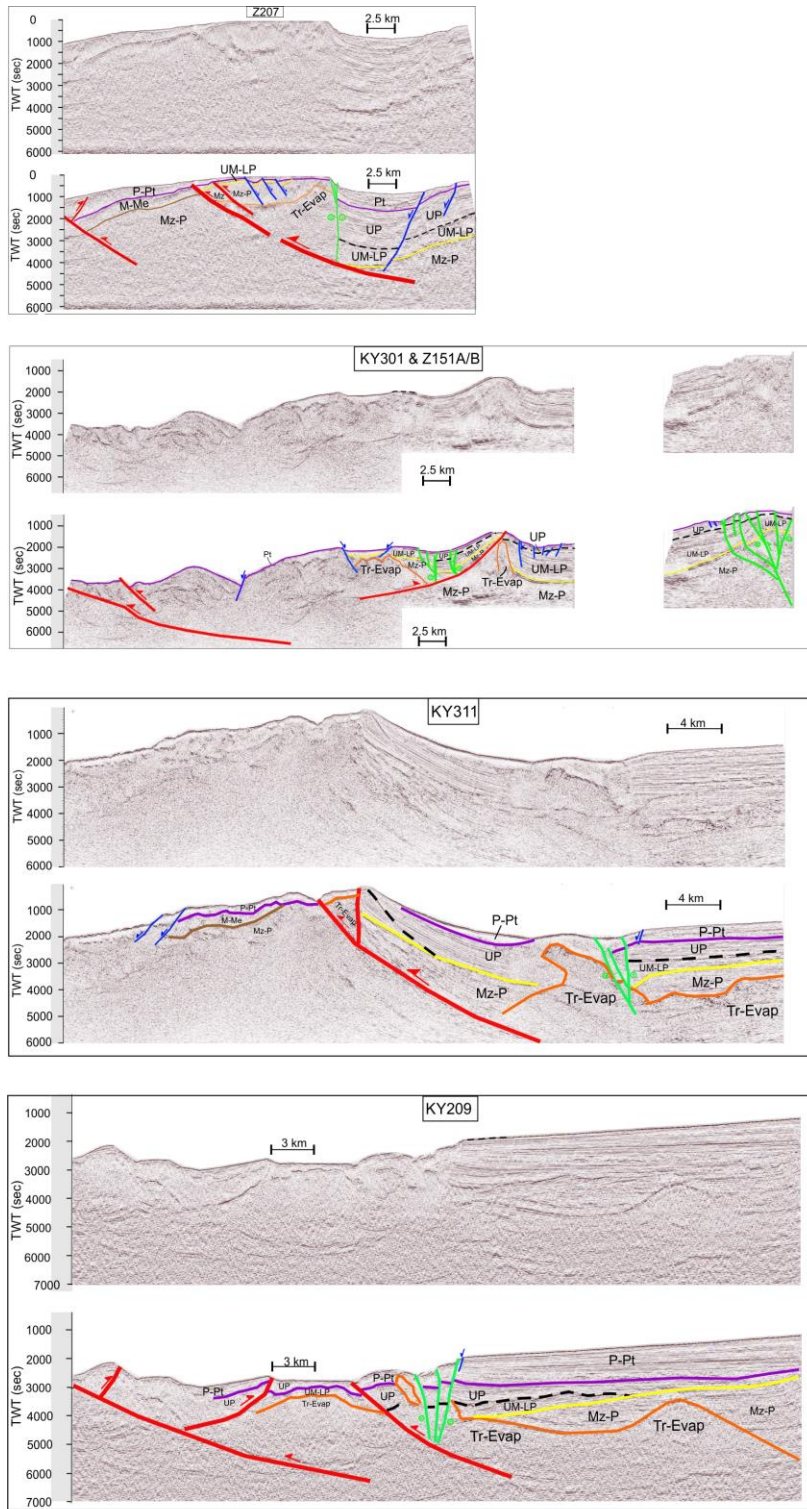
916

917

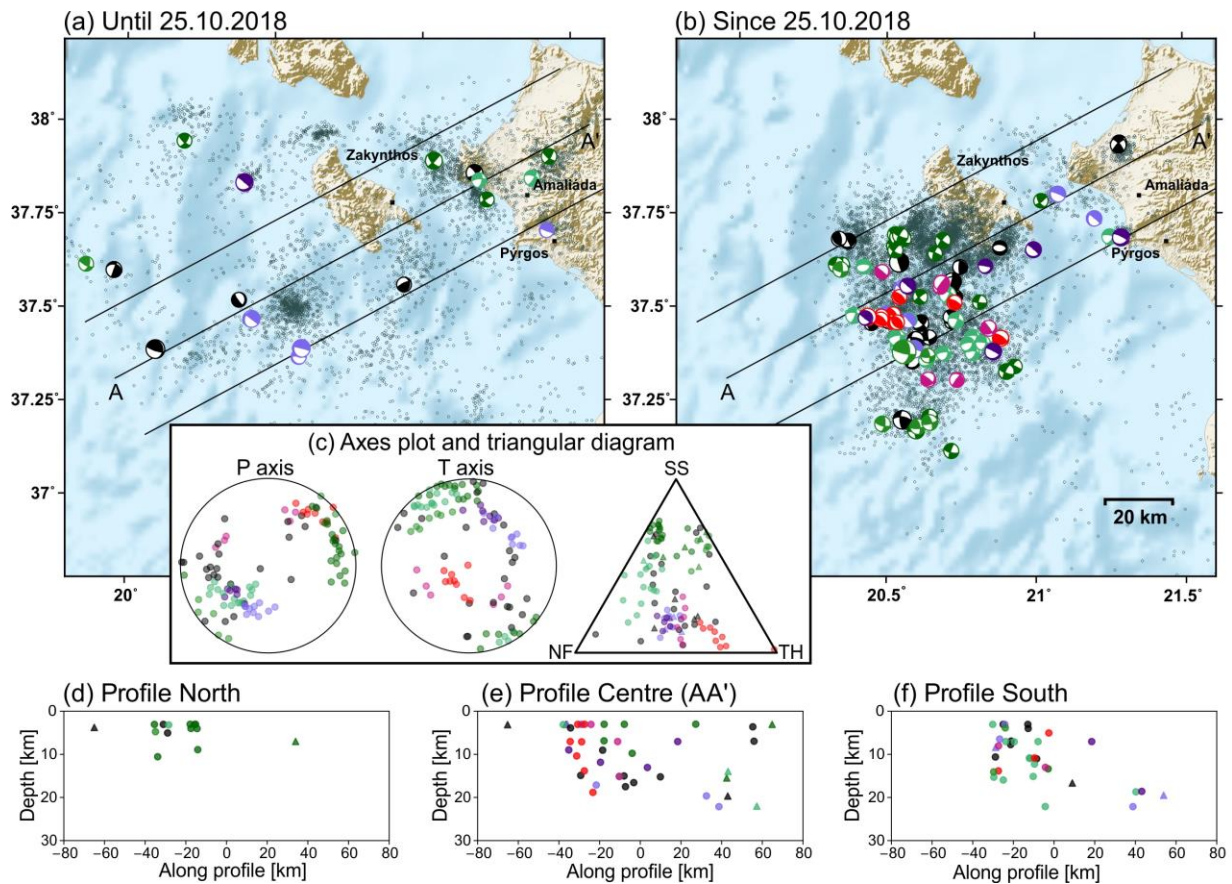
918



919
 920 **Figure 3. Spatial and temporal distribution of the ZES.** Map-view and cross-section of the relocated
 921 ZES over three distinct time-intervals: **a**, January 1st, 2014 to May 31st, 2016; **b**, June 1st, 2016 to October
 922 25th, 2018; **c**, October 25th, 2018 to May 30th, 2019. Earthquake activity in each panel is projected along
 923 the profile A-A' (70 km either side of the profile) and colour-coded according to time (see legend).
 924 Seismic events have horizontal and vertical locations errors <5 km and RMS <0.5 sec. Black dashed-lines
 925 in map-view and cross-section indicate the depth-to-the-top of the plate-interface (from Halpaap et al.,
 926 2019) while red star indicates the M_w 6.9 epicenter. The seventeen focal mechanisms obtained within the
 927 pre-October 25th 2018 sequence are colour-coded according to fault type (red=thrust, blue=normal,
 928 green=strike-slip). Locations i-iv indicate prominent earthquake clusters (see text for discussion).
 929 Z=Zakynthos Island. Bathymetry derives from <https://www.gmrt.org/>.
 930

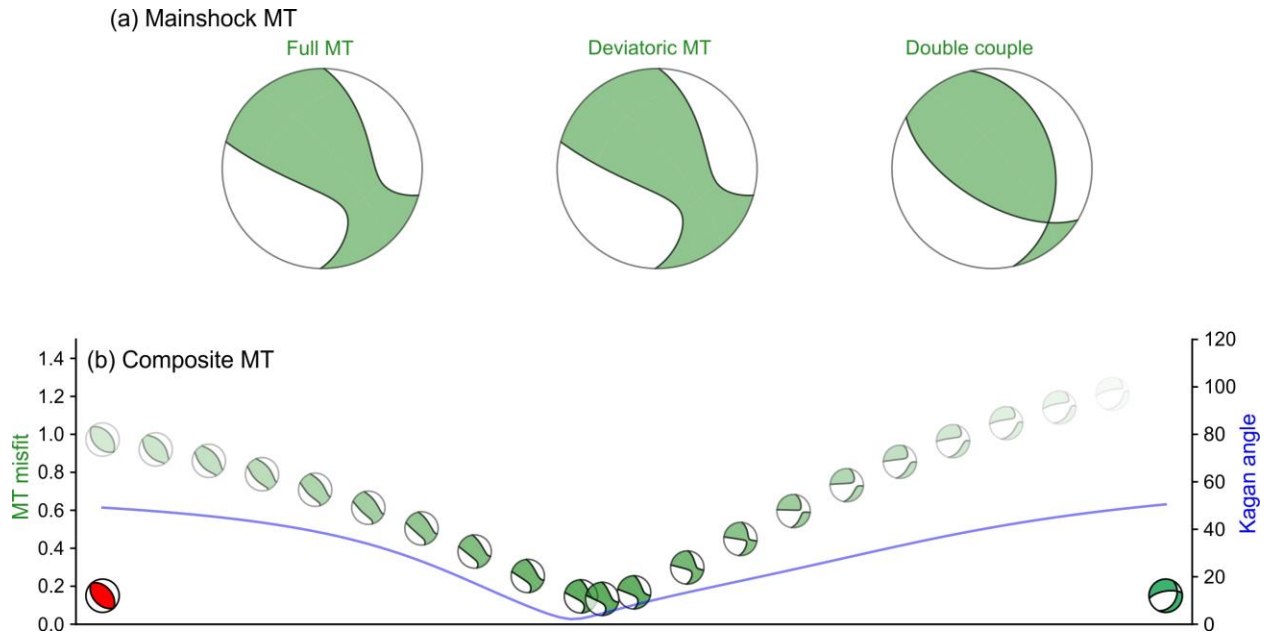


931
 932 **Figure 4. Long-term faulting and kinematics within the ZES.** Migrated (top) and re-interpreted
 933 (bottom) sections of MCS seismic-reflection profiles Z207, KY301-Z151A/B, KY311 and KY209 from
 934 Wardell et al. (2014). Normal (blue), thrust (red) and strike-slip (green) faults are colour-coded as per
 935 focal mechanisms presented in Figures 3 and 5. P-Pt=Pliocene-Pleistocene, UP=Upper Pliocene, UM-
 936 LP=Upper Miocene-Lower Pliocene, M-Me=Miocene and Messinian, Mz-P=Mesozoic-Paleocene, Tr-
 937 Evap= Triassic evaporates (orange). The seismic stratigraphy is adopted from Kokalas et al. (2013).



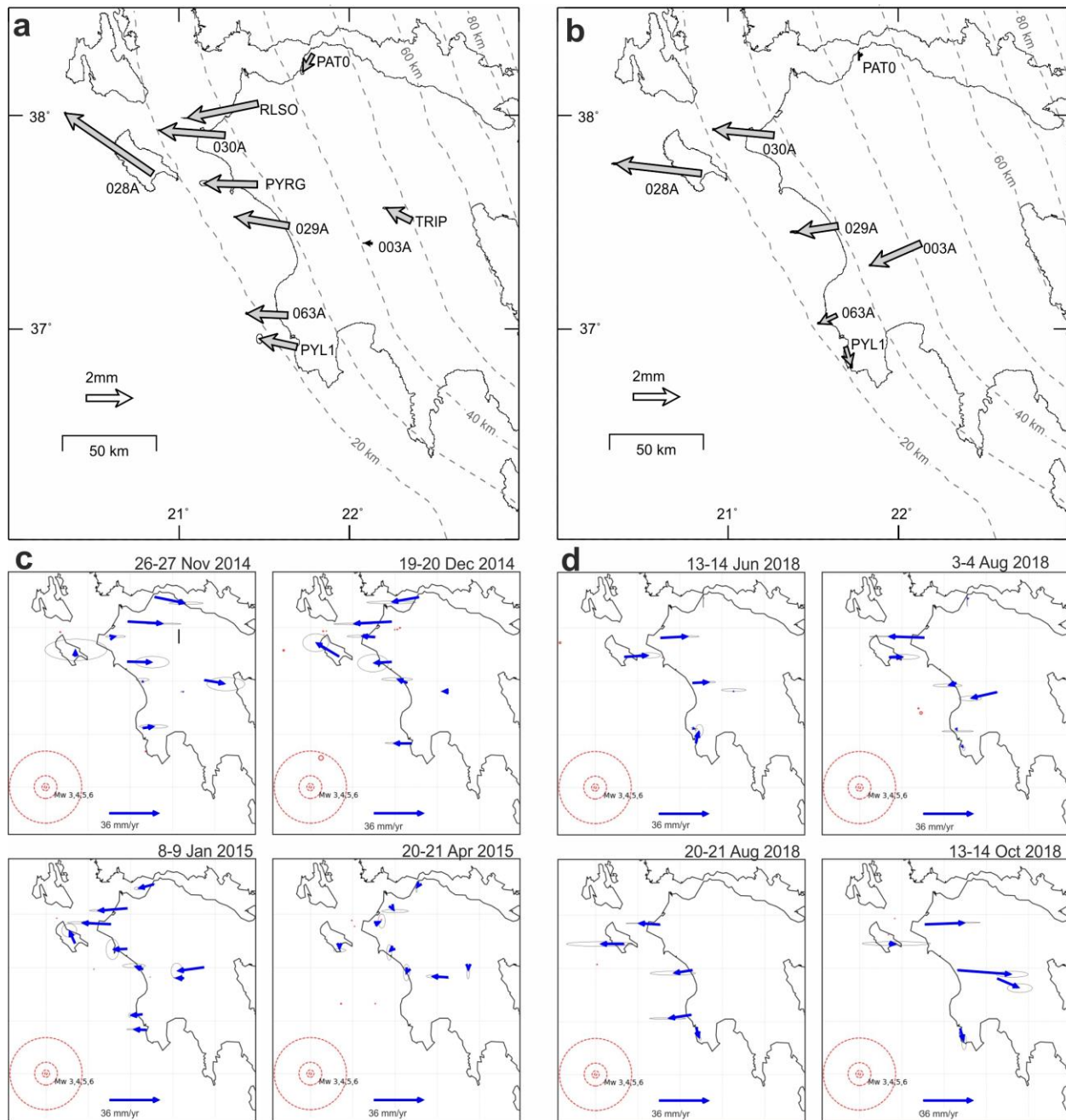
938
 939 **Figure 5. Focal mechanisms within the ZES.** Map-view (a-b) and cross-sections (d-f) of 102 focal
 940 mechanisms from the ZES. Beachballs are colour coded according to 8 clusters of earthquakes with
 941 similar focal mechanisms, with the colours recalling the fault type (red=thrust, blue=normal,
 942 green=strike-slip and associated shadings when events span various types of faulting; black is used for
 943 solutions with unclustered focal mechanisms; see Supplementary Fig. S5 for details). The triangle
 944 diagram in (c) denotes the kinematics of events analysed by means of pressure (P) and tension (T) axes
 945 orientations and a triangular diagram after Frohlich (1992). Circles in c-f indicate events that occurred
 946 during the aftershock sequence while triangles represent events that occurred prior to the main event (Oct.
 947 25th, 2018). The relocated ZES seismicity is indicated in (a) and (b) with small grey circles.

948
 949
 950
 951
 952
 953
 954
 955
 956
 957
 958
 959
 960
 961
 962
 963



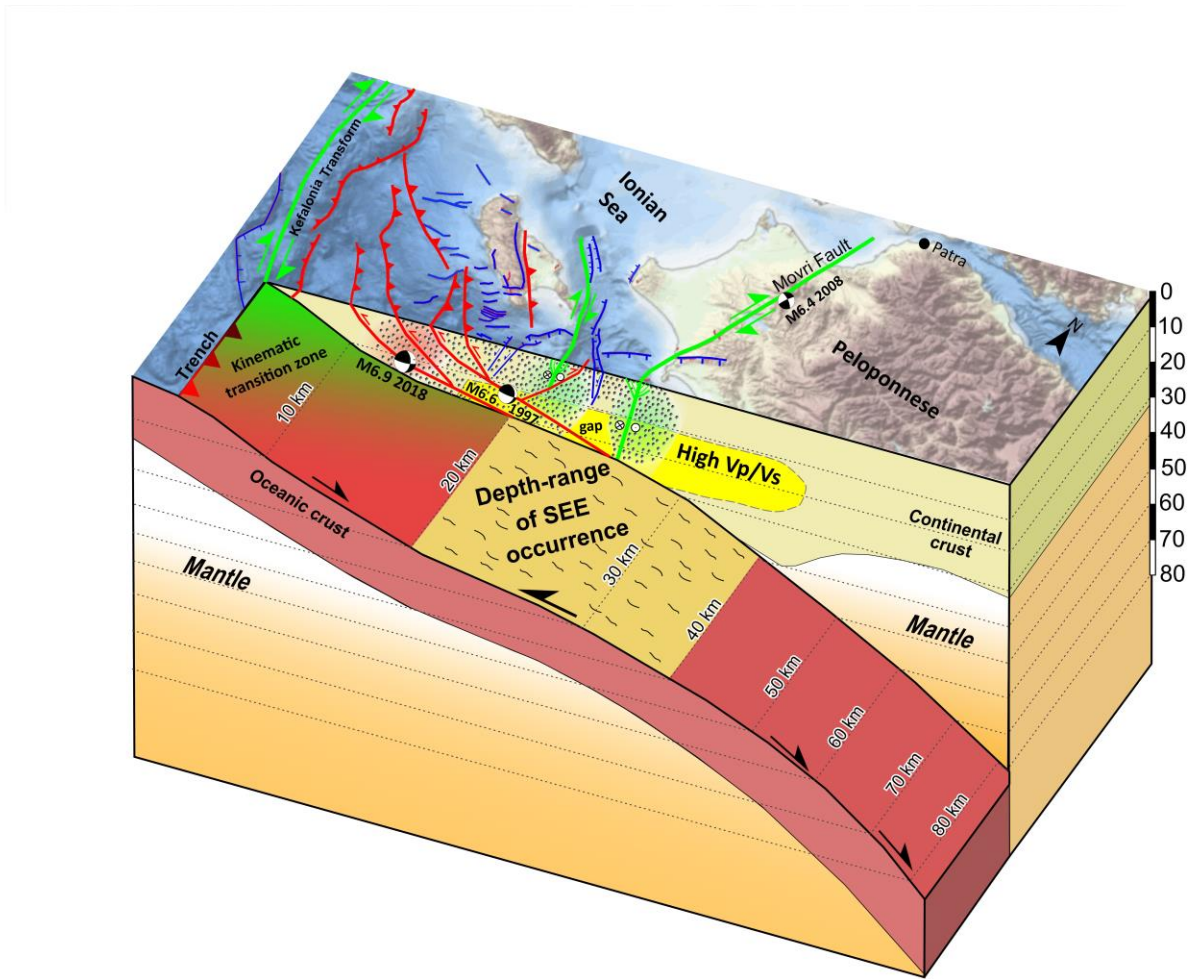
964
965
966
967
968
969
970
971
972
973
974
975
976
977
978
979

Figure 6. Mainshock moment tensor obtained (a) Full moment tensor (MT) obtained for the mainshock and its deviatoric and pure double couple (DC) components. (b) Overview of composite mainshock moment tensor obtained superposing two moment tensors with different contributions, one for an earthquake (5.11.2018 12:21) of the red thrust cluster and one for an earthquake (18.11.2018 5:18) of the sea-green cluster; focal sphere are plotted with lower transparency as they better fit the mainshock full MT (a blue line, denoting the Kagan angle among double couples of the mainshock and composite MTs, shows that the DC is also well reproduced for the suggested MT composition).



980
 981 **Figure 7. Slow-slip events along the termination of the HSS.** Transient signals of surface
 982 deformation as derived from the analysis of GPS timeseries. Cumulative trench-ward transient
 983 displacements, together with their uncertainties (1-sigma), observed between **a**, 24.09.2014-
 984 20.03.2015 and **b**, 14.05.2018-25.10.2018 **c**, and **d**, Snapshots of the daily velocity evolution of
 985 the transient GPS signal with respect to the long-term velocity of each station for the periods
 986 corresponding to transient signals of (c) and (d), respectively. The upper-left panels in (c) and (d)
 987 show the network-wide acceleration observed before the reversal of the velocity vectors (Fig.
 988 2e). Contours in a-b mark the top of the plate-interface (Halpaap et al., 2019).

989
 990



991 **Figure 8. 3D-views of the deformation processes operating at the HSS termination.**
 992 Schematic block diagram illustrating the spatial distribution of the seismic (earthquake) and
 993 aseismic (SSEs) deformation at the western-end of the Hellenic subduction margin as recorded
 994 during the 5 years preceding the M_w 6.9 Zakynthos Earthquake. Faults are colour-coded
 995 according to fault type (red=thrust, blue=normal, green= strike-slip) as per Figs 1, 3 and 4. The
 996 high V_p/V_s zone and the plate-interface contours derive from Halpaap et al. (2019). Shading
 997 around earthquakes highlights the larger clusters. The cross-section presented here partly reflects
 998 the seismic-reflection line KY301-Z151A/B presented in Figure 4 (for location see Fig. 1). The
 999 black moment tensor solutions indicate the two $M > 6$ earthquakes that ruptured two distinct thrust
 1000 faults of the study area (see caption of Fig. 1 for details). Offshore bathymetry derived from
 1001 EMODnet (<https://portal.emodnet-bathymetry.eu/?menu=19>).

Earthquake-swarms, slow-slip and fault-interactions at the western-end of the Hellenic Subduction System precede the M_w 6.9 Zakynthos Earthquake, Greece

**Vasiliki Mouslopoulou^{1,3*}, Gian-Maria Bocchini², Simone Cesca³,
Vasso Saltogianni³, Jonathan Bedford³, Gesa Petersen³,
Michael Gianniou^{4,5}, Onno Oncken³**

¹National Observatory of Athens, Institute of Geodynamics, Athens, 11810, Greece
(vasiliki.mouslopoulou@noa.gr)

²Ruhr University of Bochum, Institute of Geology, Mineralogy and Geophysics,
Germany (Gian.Bocchini@rub.de)

³GFZ Helmholtz Centre Potsdam, German Research Centre for Geosciences,
Telegrafenberg 14473 Potsdam, Germany
(cesca@gfz-potsdam.de; salto@gfz-potsdam.de; jbed@gfz-potsdam.de; gesap@gfz-potsdam.de; oncken@gfz-potsdam.de)

⁴Hellenic Cadastre, Athens, 15562, Greece (mgianniu@ktimatologio.gr)

⁵University of West Attica, Athens, 12243, Greece (mgianniou@uniwa.gr)

Contents of this file

Text S1 to S6
Figures S1 to S17
Tables S1 to S6

Additional Supporting Information (Files uploaded separately)

Tables S3 & S4
Movies S1 to S3

Introduction

The following text (Text S1-S6) and data (Supplementary Figs S1-S17, Supplementary Tables S1-S6 and Movies S1-S3) present details on the calculation of various seismic parameters (b-value, magnitude of completeness, etc.), calculation of moment tensor solutions, analysis and modeling of GPS data and analysis of fault kinematics, complementing those included in the article: ‘Earthquake-swarms, slow-slip and fault-interactions at the western-end of the Hellenic subduction system precede the M_w 6.9 Zakynthos Earthquake, Greece’.

In detail:

Text S1: Calculation of b-value, M_c and conversion of M_L to M_w

Text S2: Earthquake relocation

Text S3: Regional moment tensor inversion, classification and decomposition

Text S4: Depth estimation using seismic array at teleseismic distances

Text S5: GPS data analysis and modeling

Text S6: Strain budget within the ZES

Figure S1: Evolution of the magnitude of completeness and b-value

Figure S2: Relocated foreshock ZES

Figure S3: Example of moment tensor inversion

Figure S4: Comparison of moment tensor solutions using various tools

Figure S5: Results of the moment tensor clustering

Figure S6: Comparison between observed and synthetic beams (part 1)

Figure S7: Comparison between observed and synthetic beams (part 2)

Figure S8: Timeseries of daily GPS coordinates

Figure S9: Zoom into the timeseries of selected GPS stations

Figure S10: Model (ii) of the evolution of the averaged GPS network velocity

Figure S11: Modeled GPS transient signal and fluid loading

Figure S12: Forward modeling of the transient displacements

Figure S13: Zakynthos 2014 and 2018 transients vs. global transients

Figure S14: Snapshots of Movie S1

Figure S15: Snapshots of Movie S1

Figure S16: Transect over which the cumulative seismic moment release has been calculated

Figure S17: Bathymetric profile along the transect A-B

Table S1: Seismic moment released and % of plate-motion

Table S2: Pick quality classes

Table S3: Attributes of all relocated earthquakes in the ZES

Table S4: The moment tensor solutions that have been obtained for 102 ZES earthquakes

Table S5: Hypocentral depths estimated for M_w 4.5+ earthquakes of the Zakynthos sequence

Table S6: Summary of the contribution of each process to the plate-convergence strain budget

Movie S1: Evolution of the monthly seismic moment distribution

Movie S2: Modeling of the fluid loading in the study area and comparison with SSEs

Movie S3: Evolution of the daily velocities of the transient GPS signal

Text S1. Calculation of b-value, M_c and conversion of M_L to M_w

B-values are here calculated for the time-period of between Jan 31st 2013 and October 31st 2019 (Fig. 2d and Fig. S1c). Although there are earthquake data for the time-period prior to 2013, here we have decided to restrict our b-value analysis to the post 2013 time-period for the following reasons: a) Prior to January 31st 2011 all reported magnitudes are duration magnitudes (M_d) and not local magnitudes (M_L). As a result, the magnitudes of completeness are significantly larger ($M_c \geq 3$) prior to Feb. 1st 2011 than in the considered time span (average of about $M_c = 2.0 \pm 0.1$) preventing, thus, any meaningful comparisons; and b) For the time period between February 1st, 2011 and December 31st, 2012 the magnitude of completeness (M_c) fluctuates significantly (see Fig. S1a), preventing the robust statistical calculation of b-values and their comparison with the subsequent time-intervals.

The magnitude of completeness (M_c) (Fig. 2b and Supplementary Figure S1) is calculated from the ‘goodness-of-fit’ test (Wiemer and Wyss, 2000), as the mean value over 1000 bootstrap runs using M_L published by the National Observatory of Athens (NOA). The b values reported in Fig. 2d are calculated as the mean value of 1000 bootstrap runs using the maximum-likelihood method (Aki, 1965; Utsu, 1965) and M_c constrained by the Goodness-of-Fit Test (Wiemer and Wyss, 2000). The events have been grouped in subsets of 500 earthquakes (with half-overlapping windows; starting from the mainshock time and going backwards in time) and the b-value for each subset is calculated (Fig. 2d and Fig. S1). The b-value for aftershocks is calculated for subsets of 1000 events. The greater number of events used for calculating b-values in the aftershock sequence obtains results which are thought to be less susceptible to possible changes in the number of events in the revised aftershock catalogue (the catalogue, as of February 2020, is still under revision). Nevertheless, the impact of such revision is minimal as the main analysis of this work concerns the period prior to the main Zakynthos Earthquake.

The seismic moment (Fig. 2c and Supplementary Table S1) is estimated by using the Hanks and Kanamori (1979) equation after converting M_L to M_w . The conversion from M_L to M_w was achieved by comparing the M_w obtained for a set of 102 events during moment tensor inversion (see Text S3) and the M_L adopted from NOA ($M_w = 0.975 * M_L + 0.323$).

Text S2. Earthquake relocation

Our preferred earthquake location software is the NLLoc (Lomax et al., 2000, 2009) that uses a non-linear location algorithm which is thought to provide more reliable solutions and hypocentre error estimates in case of ill-conditioned locations such as those encountered within the ZES. To reduce location errors and enhance the quality of the hypocentral solutions, we used only those phases from 30 stations located along the western coast of Peloponnese and the islands of Zakynthos and Kefalonia (22 HUSN seismographs and 8 temporary stations installed in western Peloponnese immediately after the mainshock; Fig. 1). The inclusion of additional seismic stations from central Peloponnese and/or northern Greece would have challenged the validity of our velocity model without reducing the azimuthal gap, because the crustal thickness between the mainshock region and central Peloponnese varies considerably (Pearce et al., 2012). Indeed, the average azimuthal gap for the analysed seismicity when all available HUSN stations are used is 212° (e.g. NOA solutions) while it is 216° when only the stations proximal to the ZES are analysed (Fig. 1; this study). We performed two runs in NLLoc to obtain the most accurate hypocentral solutions. The second run was performed to include travel-time residuals obtained from the first run. The inclusion of these residuals aims to correct for deviations from the 1-D velocity model at each station and improve the final solutions.

For the relocation we used a constant V_p/V_s ratio of 1.80 in accordance with other seismological studies in the area (Kassaras et al., 2016; Haddad et al., 2020). The earthquake catalogue and P and S phase picks herein were downloaded from the NOA website (<http://bbnet.gein.noa.gr/HL/>); last accessed in May 2019 for the period before the mainshock and November 2019 for the aftershocks. Furthermore, as of February 2019 the National Observatory of Athens has slightly changed the pick class qualities and associated errors for the standard routine earthquake analysis (Table S2). All relocated earthquakes are presented in the Supplementary Table S3.

Text S3. Regional moment tensor inversion, classification and decomposition

Regional moment tensor inversion has been performed for the mainshock and more than 100 earthquakes in the mainshock focal region following two full waveform-based approaches, using the Kiwi tools (Cesca et al., 2010, 2013) and Grond (Heimann et al. 2018) software. Both approaches are based on the fit of 3-components full waveforms and, in case of the first approach, the fitting of amplitude spectra. For this analysis we used regional broadband data from stations pertaining to the following networks: GE (GEOFON, 1993), IU (Albuquerque Seismological Laboratory (ASL)/USGS, 1988), II (Scripps Institution of Oceanography, 1986), G (IPGP and EOST, 1982), MN (MedNet Project Partner Institutions, 1990), IV (INGV Seismological Data Centre, 2006), HT (Aristotle University of Thessaloniki, 1981), HL (National Observatory of Athens, 1997), HP (University of Patras, 2000), HA (University of Athens, 2008), AC (Institute of Geosciences, Energy, Water and Environment, 2002), 4A (INGV, 2009), X5 (Sokos, 2015). Data and metadata have been downloaded using the FDSN web services of Orfeus, INGV, NOA, IRIS and Geofon. Seismic data are restituted, integrated to displacement, demeaned, detrended and rotated to a radial-transversal-vertical coordinate system. Data quality have been manually assessed, and a number of traces have been removed, either because containing saturated waveforms, data gaps, large noise and/or overlap with seismic signals of other events. For each earthquake, we defined a range of epicentral distances and a frequency band for the inversion, based on the catalog magnitude. For the first approach using the Kiwi tools, the general choice was as follows: The epicentral range of distances have been fixed to 150-500 km, 75-400 km, 50-300 km and 30-300 km for events with magnitude above M_I 6, M_I 5-6, M_I 4-5, and below M_I 4, respectively. Similarly, the following four frequency bandpass filters have been used for the four ranges of magnitudes, respectively: 0.010-0.040 Hz, 0.025-0.050 Hz, 0.035-0.070 Hz and 0.040-0.080 Hz. For the second, independent approach using Grond, epicentral distances of 80-400 km and a frequency band of 0.02-0.07 Hz were considered. For both approaches these parameters have been slightly modified for few events, especially during the first hours of the sequence when signals of different earthquakes overlap, in order to improve the fit.

For the moment tensor inversions based on the Kiwi tools (Cesca et al., 2010), we use a pure double couple (DC) constraint for all events. Inversions are performed in two following steps, first fitting 3-component full waveform amplitude spectra to resolve the scalar moment, centroid depth, strike, dip and rake, but not the focal mechanism polarity (Cesca et al., 2010) and later in the time domain, to resolve the focal mechanism polarity and horizontal shifts of the centroid location. An example of the inversion results after these two inversion steps is shown in Fig. S3. We also tested the inversion using a full moment tensor configuration (Cesca et al., 2013), but judged that the non-DC terms are not robustly resolved for many earthquakes, due to the limited

azimuthal coverage and the weak magnitude of the target earthquakes. Therefore, in this work, a full MT solution is only discussed for the mainshock, where we obtain 72% DC, 18% CLVD and 10% isotropic component. The presence of a significant non-DC component and the ENE-WSW orientation and negative sign of the CLVD major axis are in agreement with reference solutions by Global CMT and Sokos et al. (2020). The second MT inversion using Grond (Heimann et al., 2018), is in this study based on the inversion of displacement traces only. An important advantage of Grond is that the moment tensor optimization is performed simultaneously simulating many station configurations using a bootstrap approach: analysing the ensemble of best solutions for different station configurations allows estimating source parameter uncertainties. Comparison of results and estimated uncertainties for selected parameters are illustrated in Fig. S4.

We processed 124 earthquakes, all those occurring in the time period 1.1.2014-31.5.2019 with local magnitude equal or larger than 4.0 and within latitudes 36.8° - 38.0° and longitudes 19.5° - 21.6° according to our relocated catalog. Good quality moment tensor solutions have been obtained for a subset of 102 earthquakes, down to a moment magnitude M_w 3.9 (Table S4). The selection of best solutions was done upon the quality of the misfit after the two inversion steps.

Focal mechanisms of the 102 solutions are classified using a clustering algorithm (Cesca, 2020), using clustering parameters $N_{min}=2$ and $eps=0.16$ (equivalent to 19.2° Kagan angle). We identify 8 clusters, representing $\sim 77\%$ of the focal mechanisms (Fig. S5). Clusters are characterized either by strike-slip mechanisms or by thrust and normal faulting mechanisms with oblique components. Two clusters located in the vicinity of the mainshock epicenter show trench parallel thrust faulting (red focal mechanisms in Fig. 5) and oblique (strike-slip to normal) mechanism (seagreen mechanisms in Fig. 5). These two types of mechanisms are observed for many early aftershocks and could thus map the geometry of faults activated during the mainshock, as found for previous complex earthquakes (e.g. Cesca et al., 2017). They also resemble the mechanisms proposed by Sokos et al. (2020) for two subfaults contributing to the Zakynthos earthquake rupture. Supposing that the two faults were active during the mainshock, their combined contribution could resemble the full MT solution of the mainshock and its non-DC component. A similar result has been shown for the 2017 Kaikoura earthquake, New Zealand (Cesca et al., 2017). Figure 6 in the main article shows how a combination of $\sim 53\%$ and $\sim 47\%$ oblique faulting can qualitatively reproduce the mainshock MT and its double couple.

Text S4. Depth estimation using seismic array at teleseismic distances

Hypocentral locations for offshore seismicity may suffer, in absence of dedicated amphibious seismic deployments, from the asymmetry of the land stations distribution and the large azimuthal gap. This problem can affect to a certain extent the analysis of the Zakynthos sequence, given the lack of local stations West of Zakynthos Island. Typically, the source parameter which is mostly affected is the source depth, which can have large uncertainties. Furthermore, there may be trade-offs among the resolved origin time, epicentral locations and depth. Here, we supplement the hypocentral relocation based on local onshore data, with an independent analysis at large distances using seismic arrays. This method has been used for the depth estimation of crustal seismicity in previous studies (e.g., Negi et al., 2017, Grigoli et al., 2018).

We stack seismic waveforms recorded at the seismic stations composing the GERES array, to construct a seismic beam, where the similar waveforms produced by a far distance earthquake (e.g. at Zakynthos) sum up constructively, in contrast to the uncorrelated seismic noise. As a result, we can obtain beams with a high signal-to-noise ratio for events of magnitude larger than Mw 4.5. We can then compare the observed beam with synthetic beams computed for the known moment tensor solution and variable source depths.

The following Figs. S6-S7 show two examples of comparison of observed and synthetic array velocity beams at the GERES array, Germany. The best depth is chosen upon a visual assessment of the fit, mostly aiming to reproduce the time delay of the pP arrival with respect to the first P onset. The pP phase travels from the earthquake focus to the surface (or the seafloor) and backward, later following a common path with the P phase. Thus the path difference among P and pP rays is the one traveled by the pP ray above the source. The pP-P delay measures the time needed for a P phase to travel two times above the hypocenter: the larger is the time delay, the larger the hypocentral depth. The absolute hypocentral depth can be directly inferred from this time delay, known the crustal velocity structure at the focal region.

In this work, we have obtained acceptable fits, and thus independent depth estimates (Supplementary Table S5), for 20 out of 24 tested events.

Text S5. GPS data, analysis and modeling

GPS data

As there are institutional/governmental restrictions associated with some of the raw geodetic data used in this study, we obtained the ITRF08 daily coordinates of 5 stations (TRIP, RLSO, PYRG, PYL1 and PAT0) available at the NEVADA Geodetic Laboratory (<http://geodesy.unr.edu/magnet.php>; Blewitt et al., 2018) and of 5 stations (063A, 003A, 028A, 030A, 029A) that belong to the HEPOS network of the Hellenic Cadastre. In both cases Precise Point Positioning (PPP) solutions were obtained. The NEVADA GPS coordinates have been processed using the GIPSY OASIS II (Jet Propulsion Laboratory, JPL) software while the HEPOS coordinates using the Canadian Spatial Reference System (CSRS) PPP software version 2.26.0. The discrepancies between the two solutions are of sub-mm level and are incorporated in the calculated velocity uncertainties (illustrated in Figure 7 in the main article and Movies S2 and S3 of the Supporting Information).

Stations ZAK2 and STRF on Zakynthos and Strofades islands, respectively, were not analyzed due to limited data (duration of timeseries <3yrs). Geodetic records of more than 3 years are required for reliable estimation of the noise level and other velocity characteristics in the GPS signal.

Optimum model solution derived from GRATSID:

Our optimum model solution (Fig. 2e) arises from a combination of the following two models: (i) pre-seismic model that derives by decomposing the pre-seismic signal only and (ii) post-seismic model that derives by decomposing the full-timeseries (1-1-2014 till 31-05-2019). This combined model was selected as the preferred solution because the 2018 transient signal was masked (Fig. S10) when we modelled the entire sequence (model ii) due to over-fitting of the large M6.9 offset on some of the stations (i.e., at station 028A these displacements reach ~40 mm and ~54 mm along the East and North component, respectively).

Forward modeling:

To better explore the origin and spatial distribution of these two transients we performed forward modelling and, assuming a homogeneous elastic half-space and using the analytical equations of Okada (1985), predicted surface displacements by assigning slip on the plate-interface (Fig. S12). The long wavelength of the GPS deformation pattern (Figure 7) suggests that aseismic slip has occurred beneath western/central Peloponnese in both SSEs of 2014 and 2018. In addition, maximum displacements are observed on Zakynthos Island, thus, implying slip at depth between mainland and the Island of Zakynthos. After testing for various displacement scenarios, we derived the best uniform-slip model for average slip of 5 mm on the plate-interface (Fig. S12c) and total geodetic moment release of 3.20×10^{25} dyne*cm (that corresponds to a $M_w \sim 6.3$ earthquake; Table S1) for each SSE, in good agreement with other transient signals globally (Supplementary Fig. S13) (i.e. Peng and Gombert, 2010), a fact that reinforces the tectonic origin of these transients. Some discrepancies observed in the north of the study area (Fig. S12), likely reflect additional distributed slip on the plate-interface or/and upper-plate faults there. Thus, the estimated average slip of 5 mm on the plate-interface should be considered as the minimum slip required for reproducing the surface deformation observed in the study area.

Characteristics of the 2014 transient (network acceleration – SSE)

Transient duration: 24/9/2014-20/3/2015: 178 days

SSE duration: 29/11/2014-20/3/2015: 112 days = $112 * 24 * 3600 = 9.6 \times 10^6$ s

Minimum moment released: 3.20×10^{18} Nm

Characteristics of the 2018 transient (network acceleration – SSE – network acceleration)

Transient duration: 14/5/2018-25/10/2018: 164 days

SSE duration: 10/7/2018-30/9/2018: 107 days = $83 * 24 * 3600 = 7.2 \times 10^6$ s

Minimum moment released: 3.20×10^{18} Nm

Text S6. Strain budget within the ZES

The relative African-Eurasian plate-motion at the western-end of the HSS is ~ 26 mm/yr (Pérouse et al., 2017). A question that arises is what percentage of the plate-motion is accommodated by each process operating at the western-end of the HSS. To answer this question we have quantified the contribution of each component of deformation (seismic and aseismic) for the period that precedes the M_w 6.9 event (Supplementary Table S6). To calculate cumulative seismic moment along the orthogonal to the plate-motion transect C-C', we first converted local magnitudes (M_L) to moment magnitude (M_w) using an empirical relationship derived in this study ($M_w = 0.975 * M_L + 0.323$) and then calculated the seismic moment (M_0) using the relation between M_0 and M_w ($M_0 = 10^{(1.5 * M_w + 16.1)}$; Hanks and Kanamori, 1979). We used calculated M_w for earthquakes for which we obtained focal mechanism solutions. The average slip (D) has been estimated using the equation $M_0 = GDA$ (Aki, 1966), where the shear modulus (G) has been assumed equal to 30 GPa (standard value for the crust), M_0 has been calculated as described above along the 20 km wide transect C-C' (Fig. S16), while the fault area (A) has been estimated according to geometry of the subducting slab (see Fig. S16).

Total geodetic moment release, as obtained from the modeled aseismic events of 2014 and 2018 (Figure S12), is estimated at 6.40×10^{25} dyne*cm (Table S1). The seismic (1.3 mm/yr; Table S6) and geodetic (2.1 mm/yr; Table S6) slip rates accommodated in the study area due to earthquake and slow-slip events, respectively, are estimated over the observational period (4.8 years).

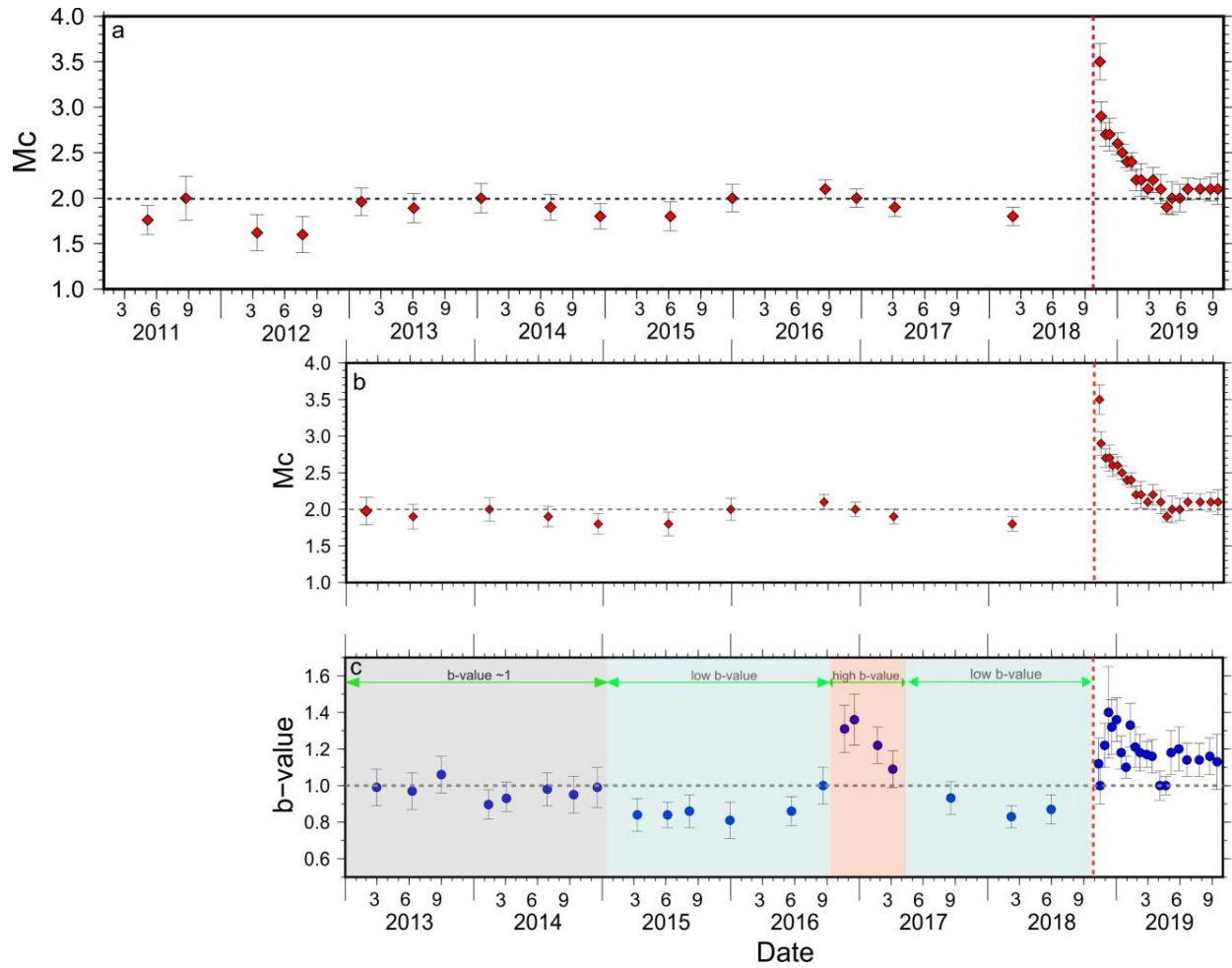


Figure S1. Graphs illustrating the evolution of the magnitude of completeness (a & b) and the b-values (c) in the study area for time periods from 1st January, 2011 to 31st October, 2019. Red dashed line indicates the timing of the M6.9 Zakynthos earthquake on October 25th, 2018. Note the fluctuating M_c values in 2012.

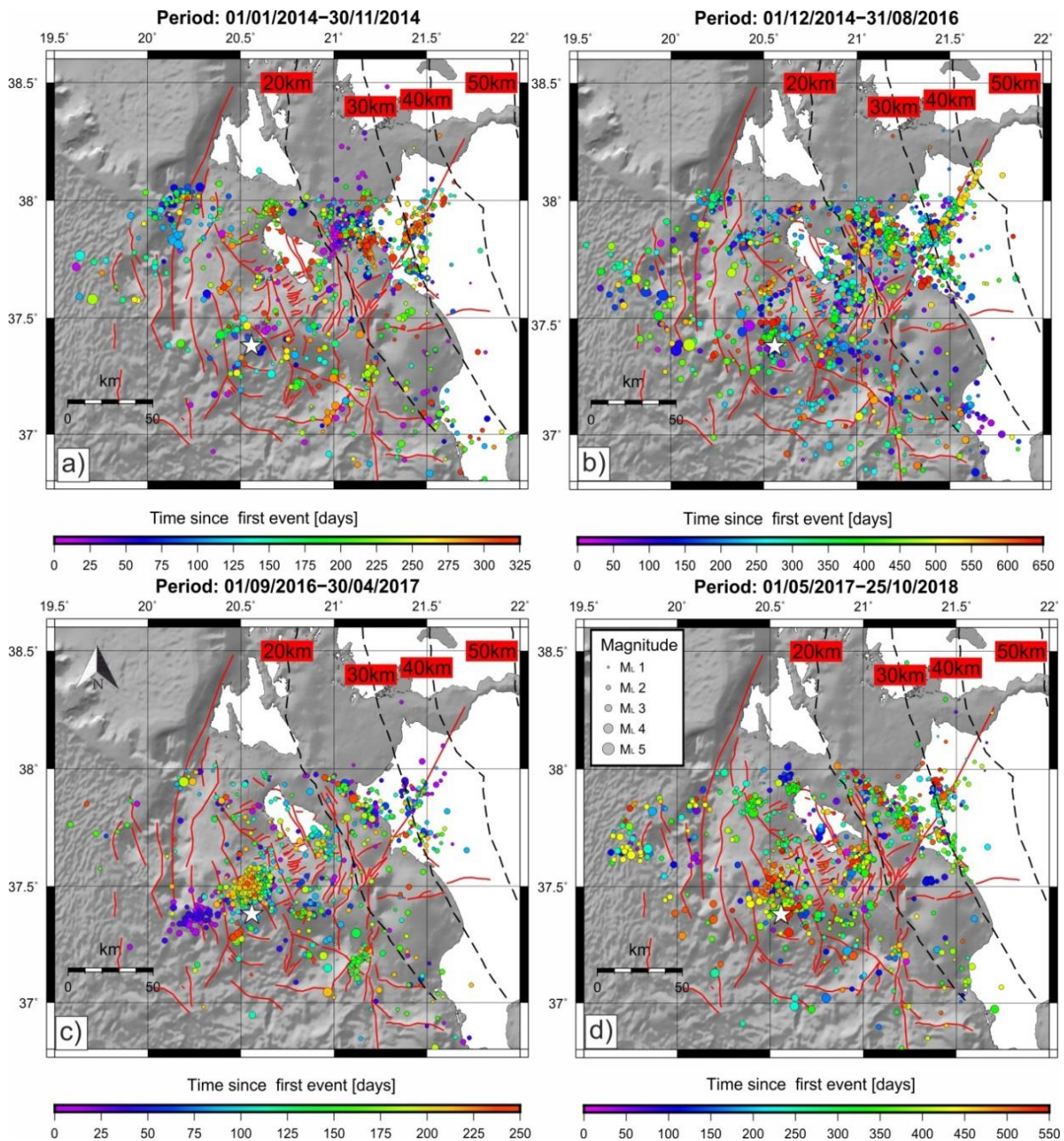


Figure S2. Map-view of the relocated foreshock ZES over four distinct time-intervals. Earthquake activity in each panel is colour-coded according to time (see legend). Seismic events have horizontal and vertical locations errors ≤ 25 km and RMS ≤ 1.5 sec. Black dashed lines in map-view and cross-section indicate the top of the plate-interface (from Halpaap et al., 2019) while white star indicates the M_w 6.9 epicentre. Bathymetry derives from <https://www.gmrt.org/>

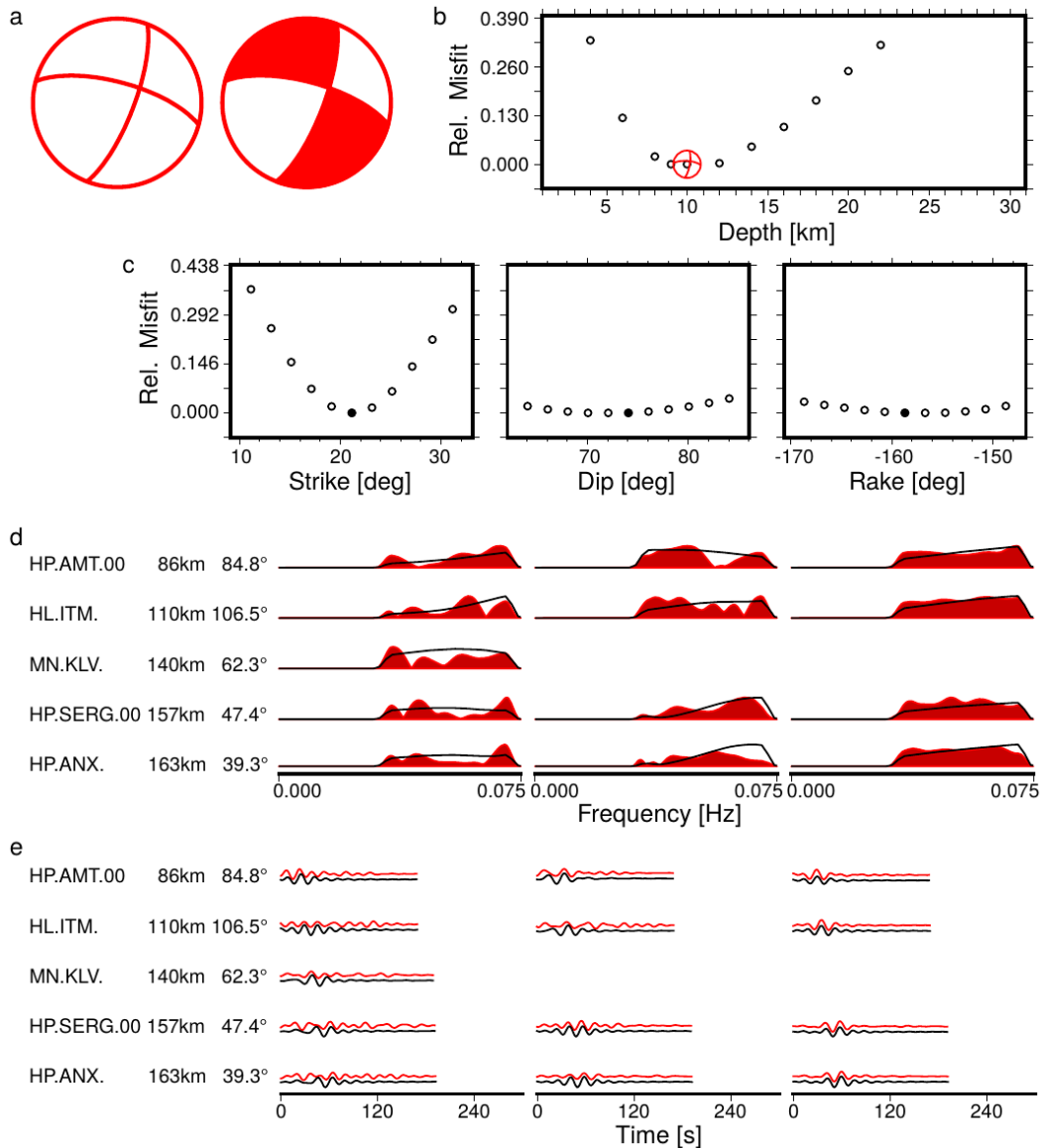
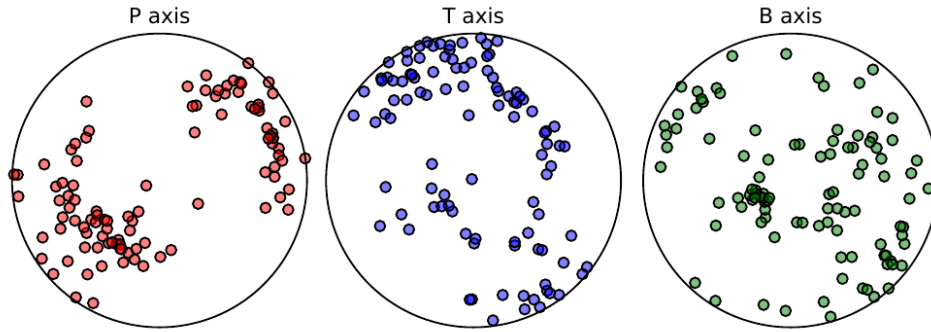


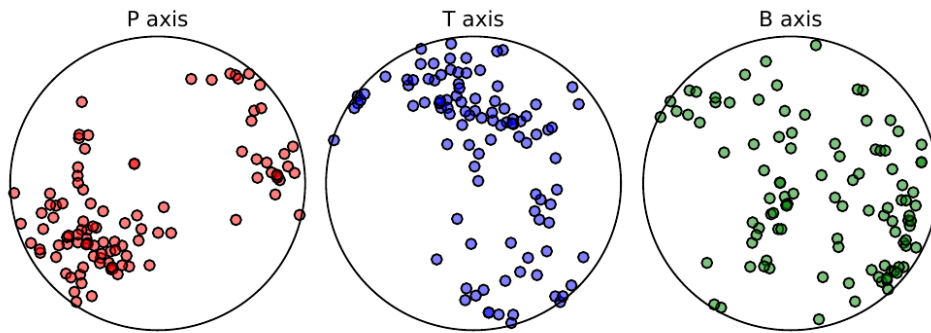
Figure S3. Example of moment tensor inversion result for the Zakynthos aftershock on 26.10.2018 at 12:11:17 UT: a, DC focal sphere after amplitude spectra inversion (white quadrants) and time domain inversion (red-white quadrants); b, relative misfit changes by perturbation of the source depth (the focal sphere denote the best solution); c, relative misfit changes by perturbation of strike, dip and rake (a solid circle denotes the best solution in each plot); d, comparison of observed (red) and synthetic (black) amplitude spectra along the vertical (left), radial (center) and transversal (right) components for selected stations (station names, epicentral distance and station azimuth are reported); e, comparison of observed (red) and synthetic (black) waveforms along the vertical (left), radial (center) and transversal (right) components for selected stations (station names, epicentral distance and station azimuth are reported).

(a) Comparison of pressure, tension and null axes

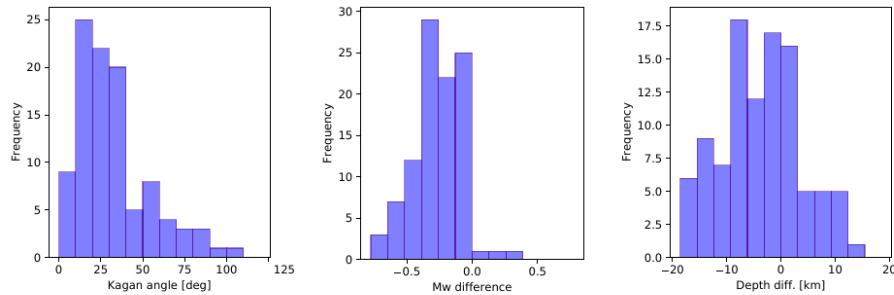
Pressure (P), tension (T) and null (B) axis resolved by Kiwi tools



Pressure (P), tension (T) and null (B) axis resolved by grond



(b) Comparison among focal mechanisms, Mw and depths



(c) Uncertainties of focal mechanisms, Mw and depths

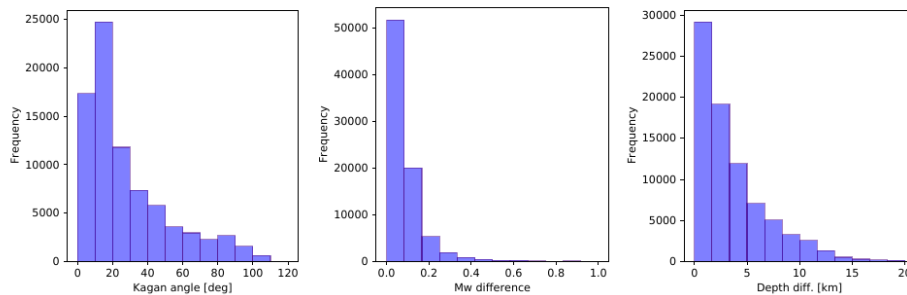


Figure S4. Comparison of solutions obtained for the same earthquakes with the Kiwi tools (Cesca et al. 2010, 2013) and Grond (Heimann et al. 2018) software, showing (a) the comparison of resolved pressure, tension, and null axes, (b) histograms with deviations among mechanisms (Kagan angle), moment magnitudes and depth estimates (values estimated by Kiwi tools minus those by Grond) and (c) histograms with uncertainties (focal mechanism orientations, moment magnitudes and depths) estimated by Grond through bootstrap: for each event, the inversion in Grond was run in parallel in 500 bootstrap chains with varying weightings of the fitting targets (station-component-phases combinations) as well as in one ,global‘ chain in which weightings

only compensate station-event distances; uncertainties of our moment tensor solutions are assessed by comparing the best solution of each event to the ten best solutions of the 100 best performing bootstrap chains and the global chain; this approach assures meaningful statistics since we consider more than 1000 bootstrap solutions.

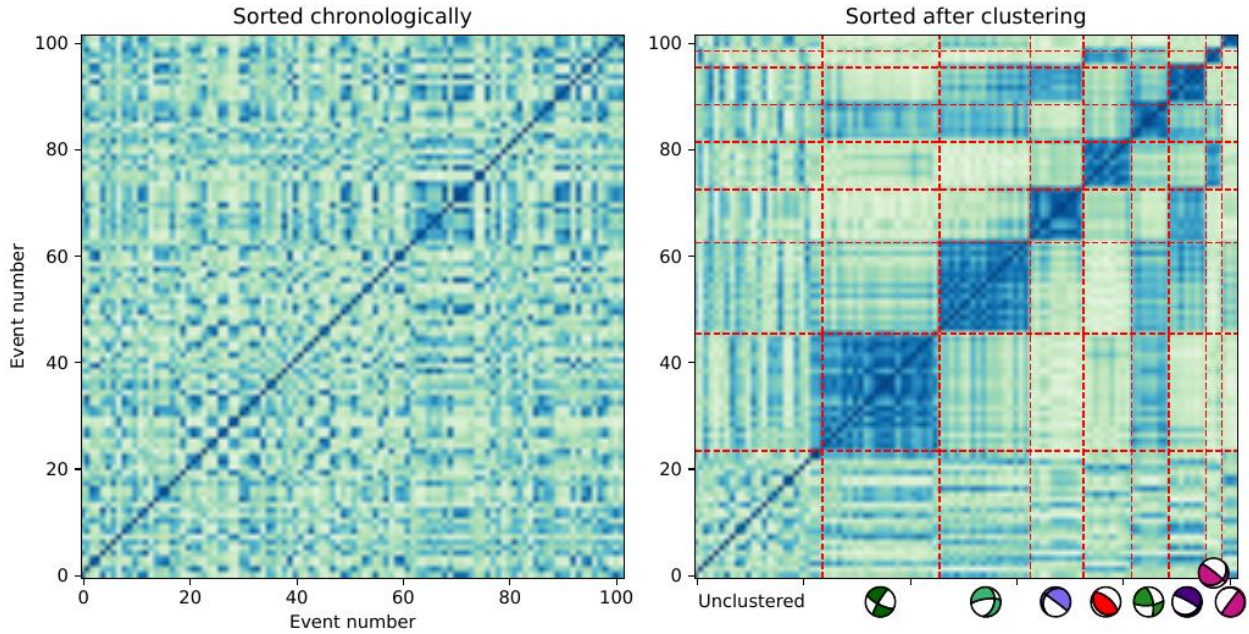


Figure S5. Results of the moment tensor clustering using seiscloud (Cesca 2020), showing similarity matrices for events sorted chronologically (left) and after clustering (right), where 8 clusters are identified (red dashed lines denote the edges of the clusters, focal mechanisms are representative (median) focal mechanisms for each clusters (colors as in Fig. 5); ~23% of the focal mechanisms remain unclustered.

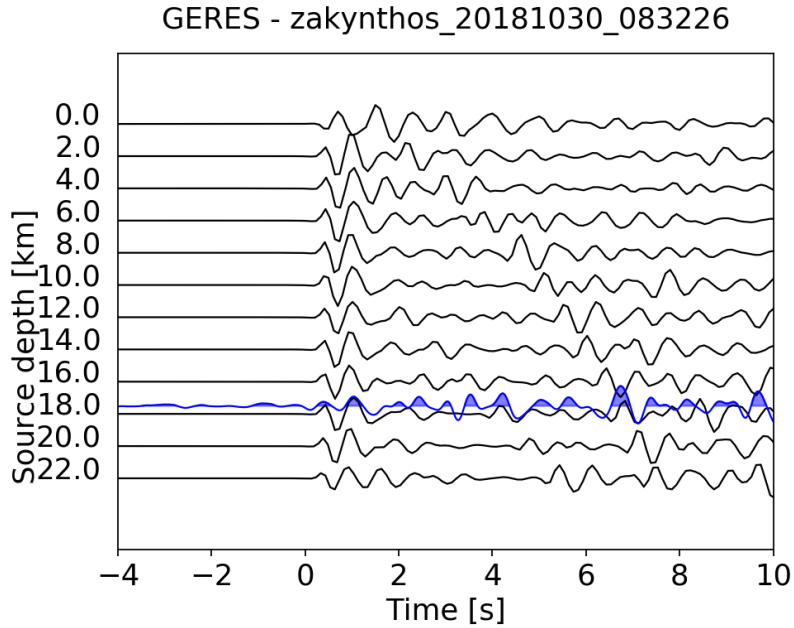


Figure S6. Comparison of the observed array beam at the GERES array, Germany, (blue) and synthetic beams for different depths (black lines), for an earthquake of the Zakyntos sequence occurring on 2018-10-30 at 08:32:26 UT. The best depth (here 17.5 km) is chosen upon a visual assessment of the waveforms fit. In particular, we aim to model the time delay of the pP arrival (here at ~ 6.5 s) with respect to the first P phase (0.0 s). Beams (here velocity waveforms) are bandpass filtered in the frequency range 0.7-2.0 Hz and normalized.

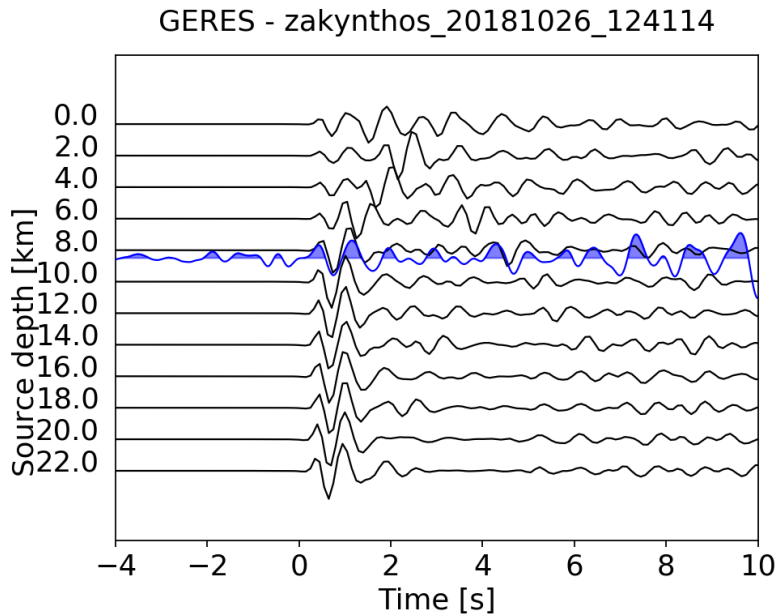


Figure S7. A second example (earthquake on 2018-10-26 12:41:14 UT) of comparison among observed and synthetic beams at the GERES array.

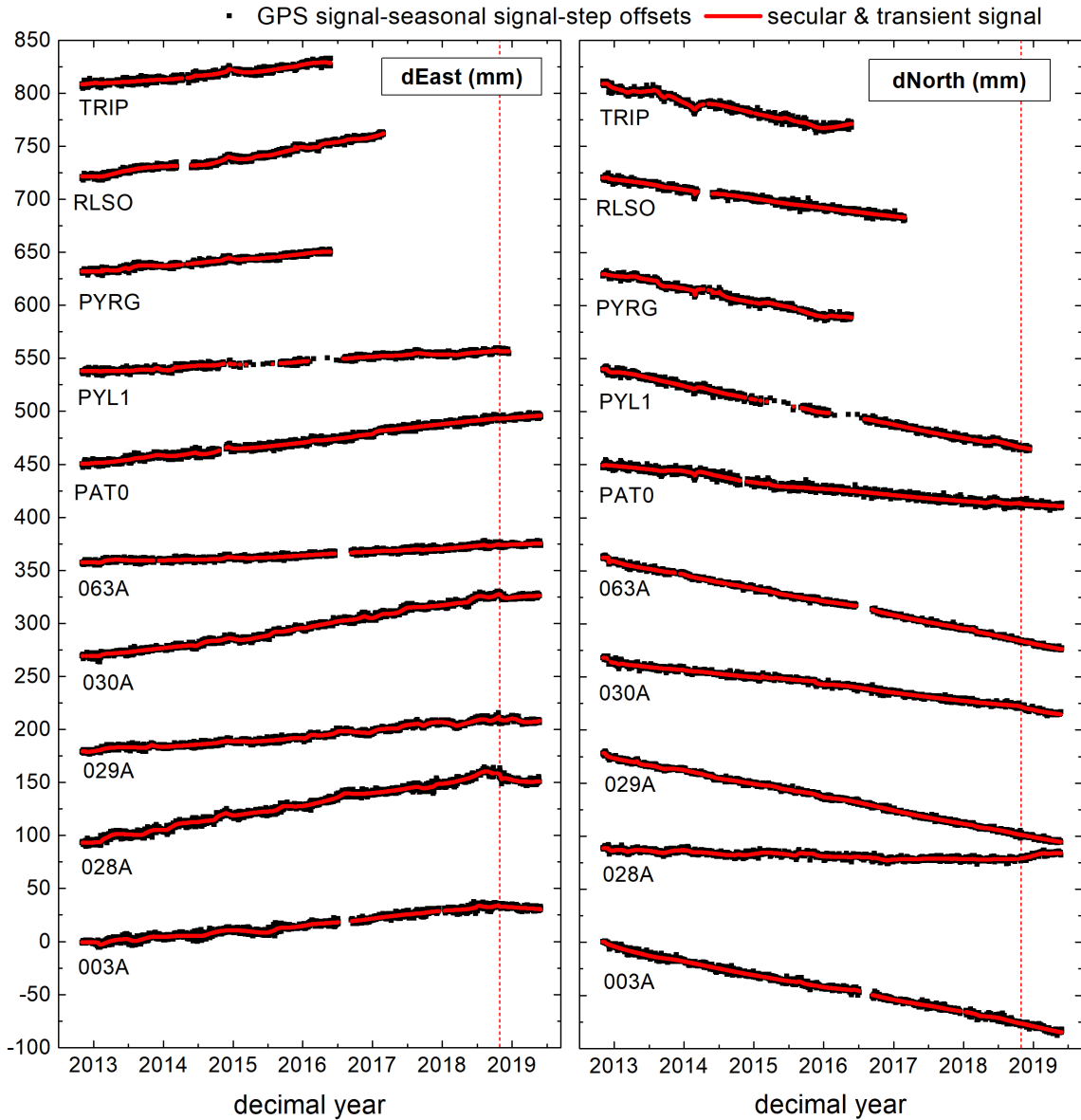


Figure S8. Timeseries of daily GPS coordinates analysed in this study along the East and North components. Filtered GPS signal, after subtracting the modeled seasonal and step-related signal, is indicated by black dots, while the decomposed transient GPS signal is indicated by the red line. Vertical red-dashed lines indicate the timing of the main-shock (October 25th, 2018).

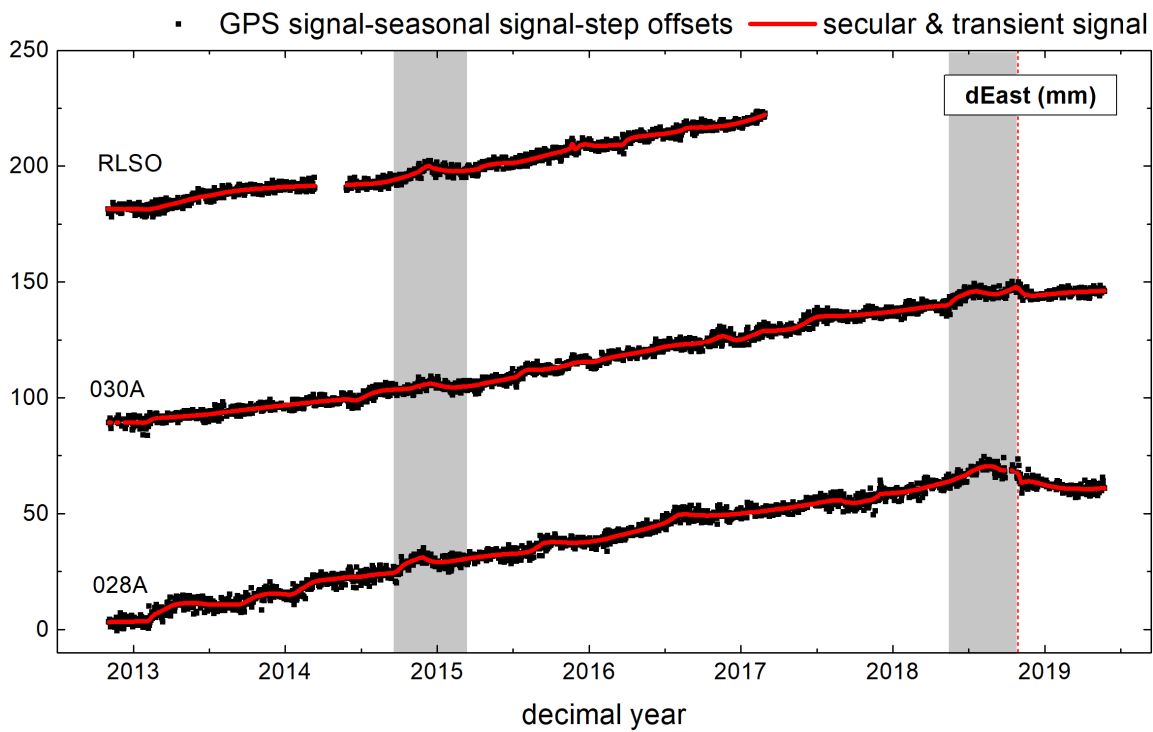


Figure S9. Similar to Figure S8, but for three selected GPS stations. Note the modelled ‘wobbles’ (Bedford et al. 2020) during the transient signals of 2014 and 2018.

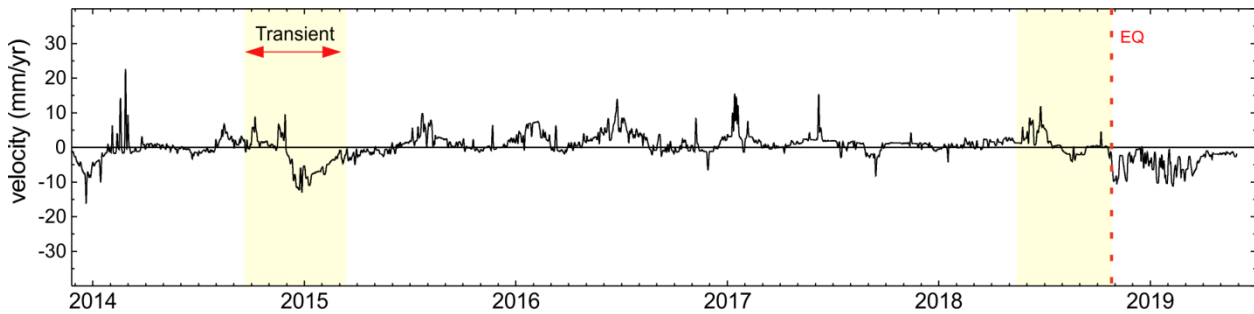


Figure S10. Evolution of the averaged GPS network velocity along the East component during the ZES, as derived from analysis of the entire pre and post-seismic GPS signal (model ii). The transient signal is clearly evident in late 2014, however, the 2018 transient signal before the mainshock (dashed red line), which is visible in Figure 2e, here is masked by the over-fitting of the seismic offset.

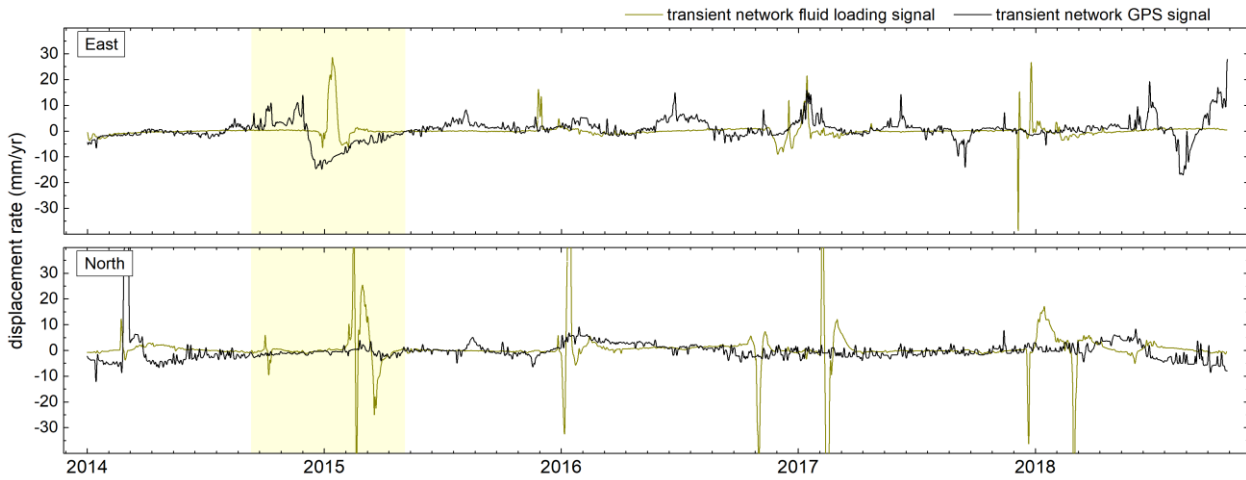


Figure S11. Modeled GPS transient signal (black line) and fluid loading (green line) signal averaged along the entire network along the East and North component. Shaded areas denote the major detected GPS transient signals.

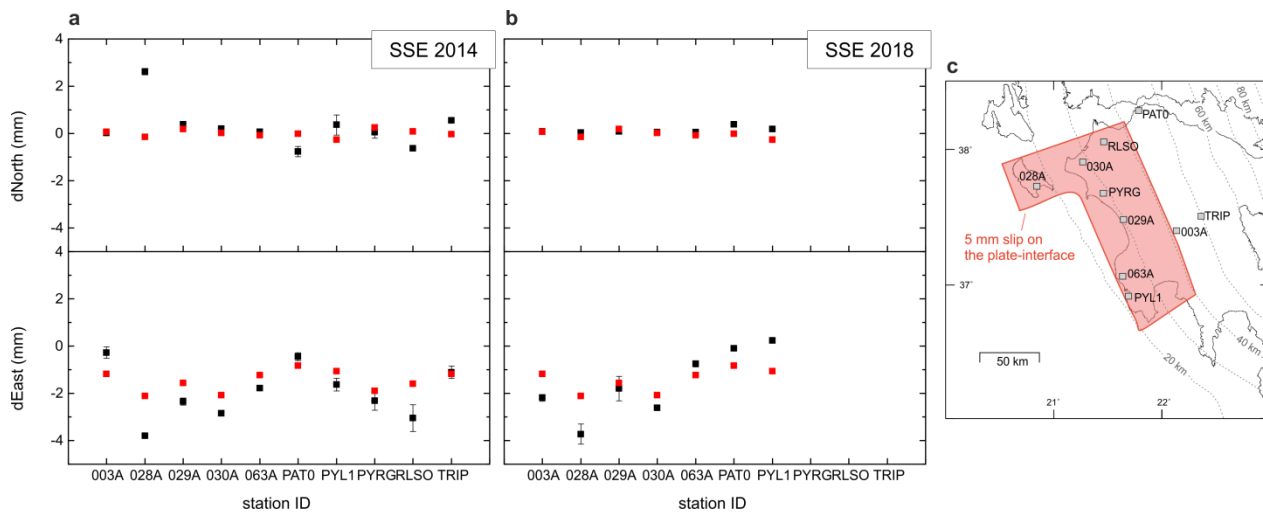


Figure S12. Results of the forward model. Predicted surface displacements (red dots) are compared with the observed GPS displacements (black dots) for the 2014 SSE (a) and the 2018 SSE (b), when slip of 5mm is assigned between the 20-40 km isodepths of the plate-interface and locally between the Zakynthos Island and Peloponnese.

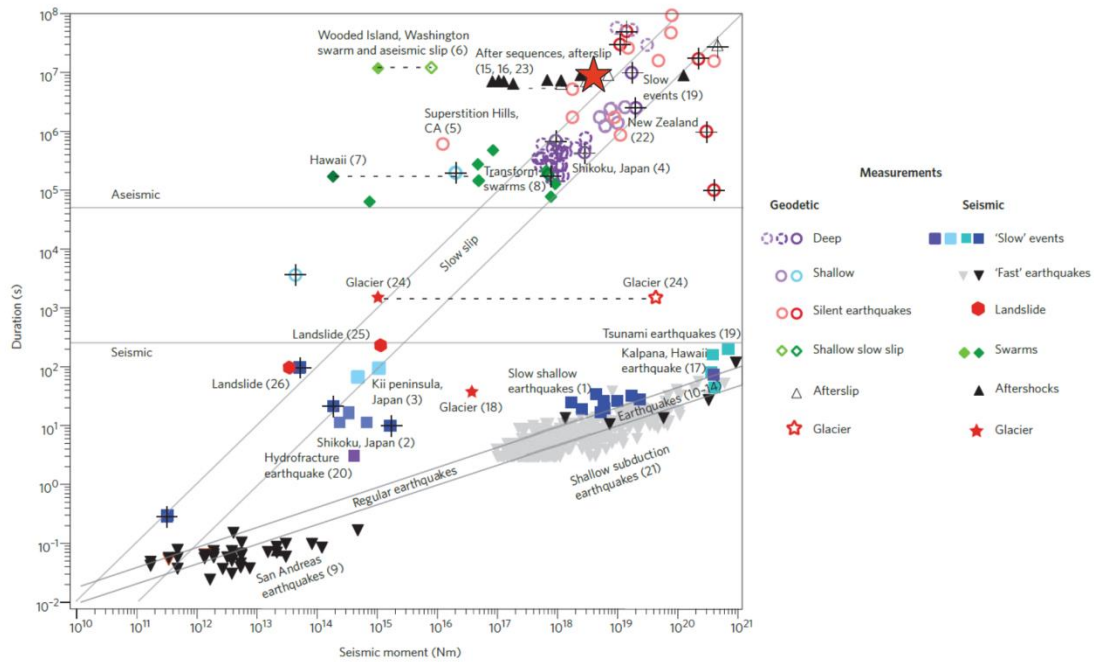


Figure S13. Graph showing the seismic moment versus source duration for a variety of fault-slip observations. Large red star indicates the 2014 and 2018 SSEs in the Hellenic margin. Figure modified from Peng & Gomberg (2010).

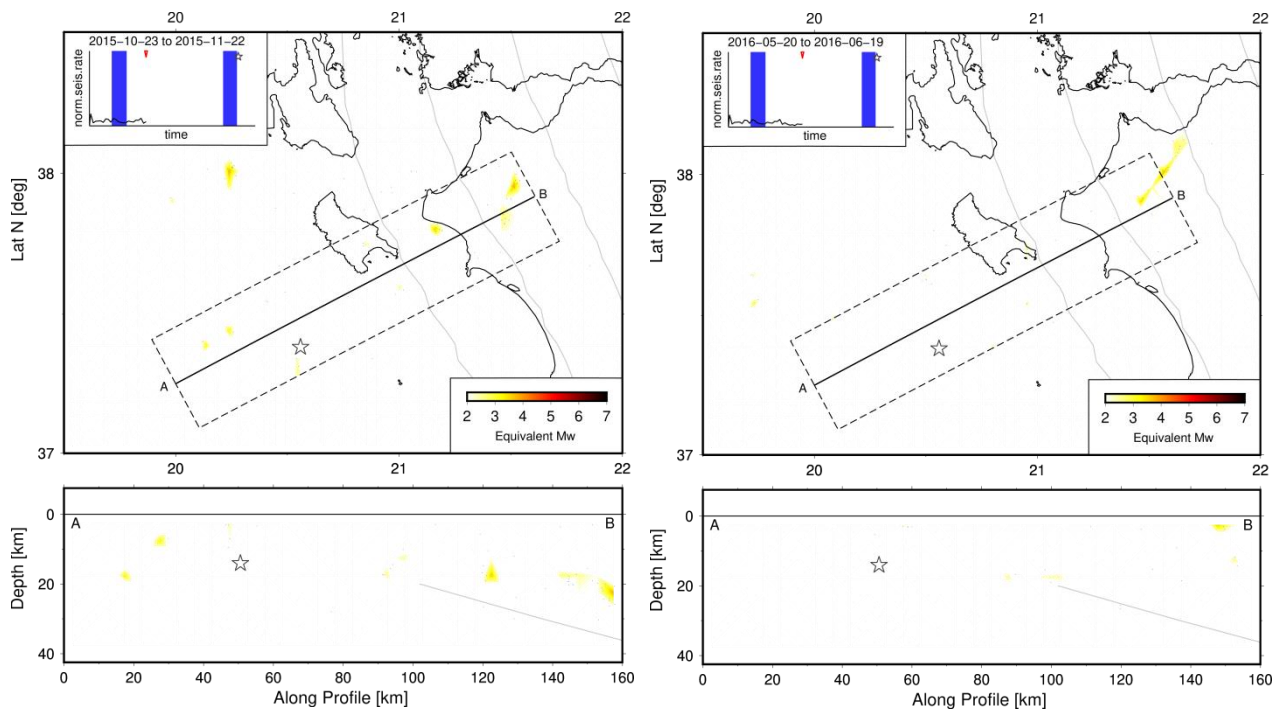


Figure S14. Snapshots of Movie S1 illustrating the seismicity recorded to delineate the Movri Fault from June to November 2015 and from May to August 2016. White star represents the epicentre of the October 25th, 2018 Mw 6.9 Zakyntos Earthquake.

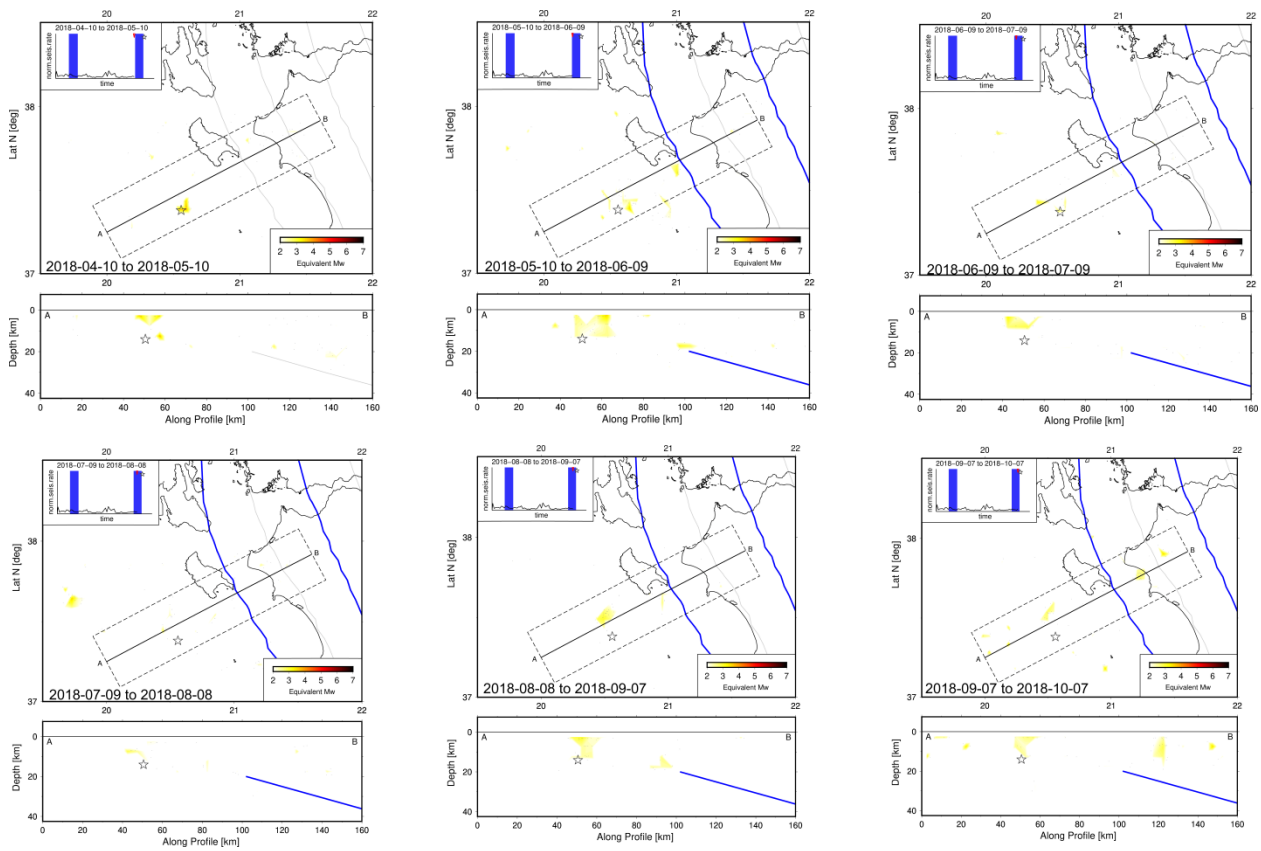


Figure S15. Snapshots of Movie S1 showing that clusters of shallow (<10 km) earthquakes occur within the epicentral area of the main Zakyntos event during the onset (May 2018) and throughout the 2nd transient. White star represents the epicentre of the October 25th, 2018 Mw 6.9 Zakyntos Earthquake.

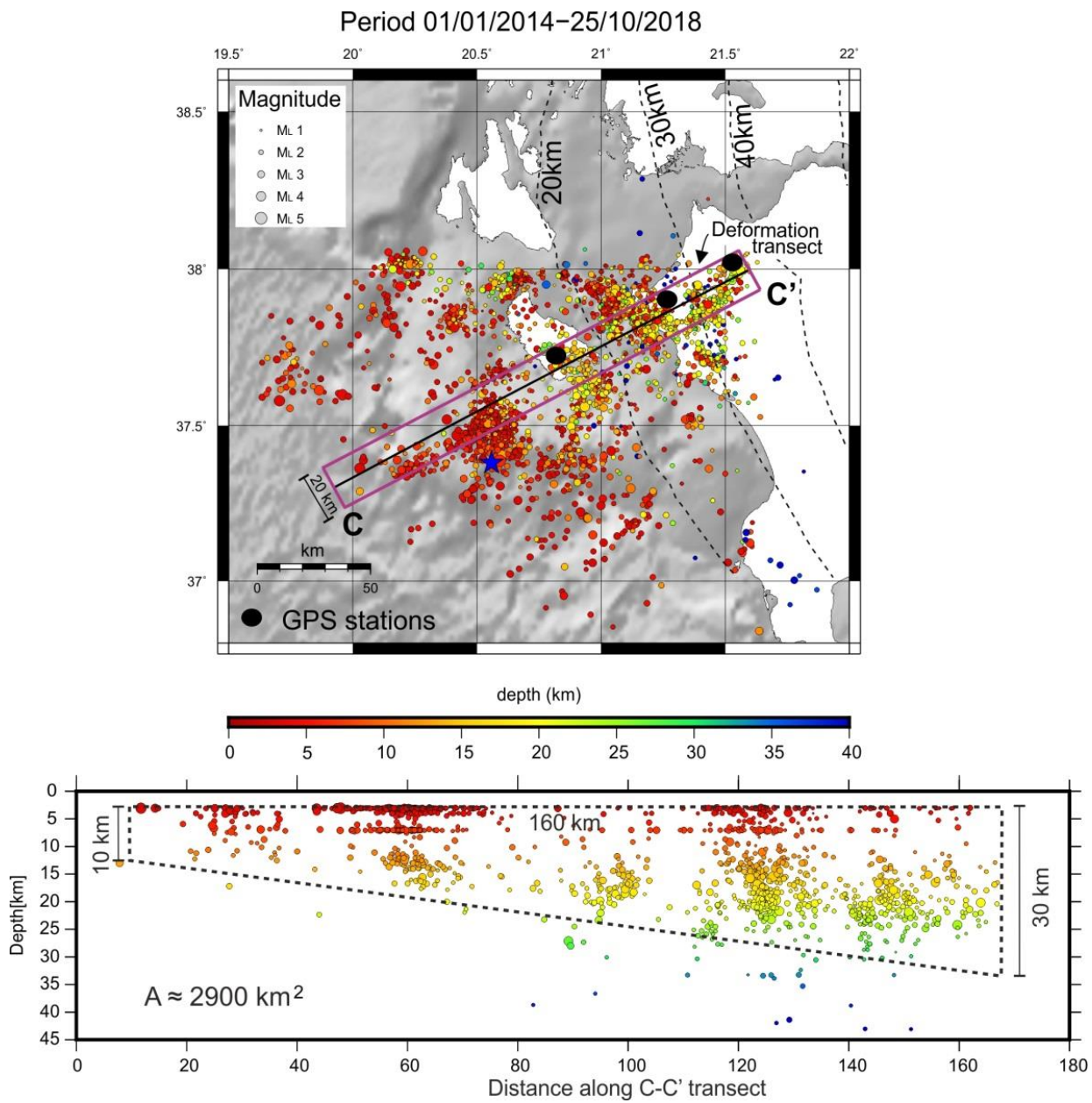


Figure S16. Transect over which the cumulative seismic (derived from earthquakes) moment release has been calculated. See text for details.

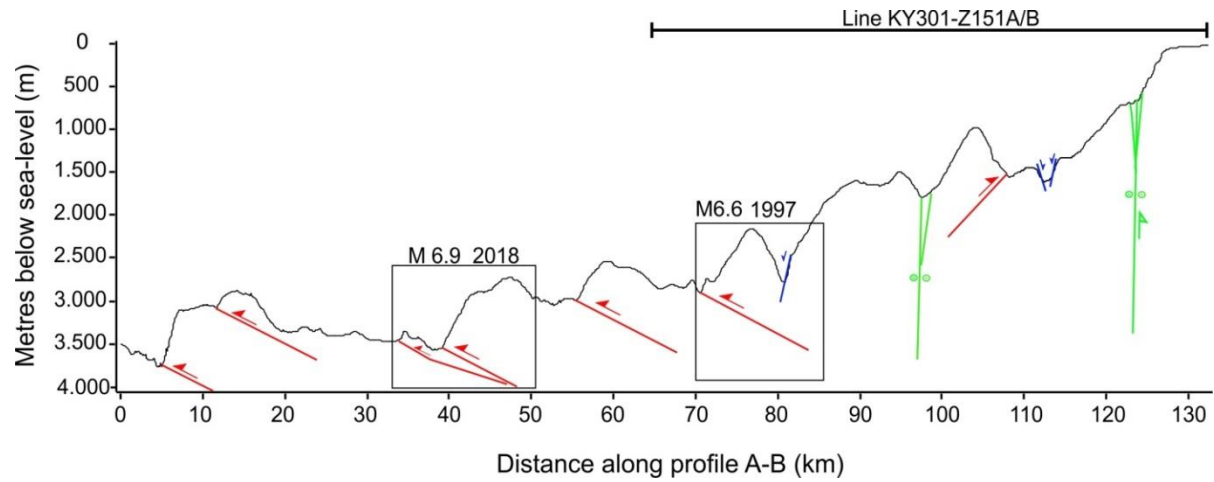


Figure S17. Bathymetric profile along the transect A-B (for locality see Fig. 1 in the main article) highlighting the control of active upper-plate faulting in the bathymetry. Faults are partly constrained by the interpretation of the seismic-reflection line KY301-Z151A/B presented in Fig. 4 and are colour coded according to Figs 1, 3, 4 and 7. The two thrust faults which are thought to have ruptured during the 1997 and 2018 M>6 earthquakes, are indicated. Vertical exaggeration x 10.

Table S1. Seismic moment released during the foreshock, aftershock and the entire ZES. Last column shows the % of the relative Eurasian-African plate-motion accommodated by each process.

Table S1	Seismic Moment (dyne-cm)	M_w	% of plate-motion
Foreshock sequence (Jan 1st, 2014 till Oct 25 th 2018)	4.95×10^{24}	5.76	5%
Aftershock sequence excluding main event (Oct 25 th , 2018 till May 31 st 2019)	2.60×10^{25}	6.24	75%
Swarm-like activity (Sept. 2016 till Apr. 2017)	3.02×10^{23}	4.95	4.5%
Entire ZES (Jan. 1 st , 2014 till May 31 st 2019)	3.13×10^{26}	6.96	-
Slow Slip event 2014	3.24×10^{25} (min)	6.3	8%
Slow Slip event 2018	3.20×10^{25} (min)	6.3	

Table S2. Pick quality classes, and associated errors in seconds, during the ZES. Data are from the National Observatory of Athens (<https://doi.org/10.7914/SN/HL>).

Before February 2019		Since February 2019	
Pick quality class	Error (sec)	Pick quality class	Error (sec)
0	0.05	0	Unset
1	0.1	1	0.05
2	0.2	2	0.1
3	0.4	3	0.2
-	-	4	0.4

Table S3. Table presenting the attributes of all relocated earthquakes in the ZES (see uploaded .csv file).

Table S4: The moment tensor solutions that have been obtained for 102 ZES earthquakes (see uploaded .csv file).

Table S5. Hypocentral depths estimated for same Mw 4.5+ earthquakes of the Zakynthos sequence, estimated upon array beam modeling.

Date	Time	Depth [km]
2015-01-02	06:16:29	6.5
2015-12-12	08:34:47	6.5
2018-10-21	23:44:55	9.0
2018-10-26	01:06:04	11.5
2018-10-26	05:48:37	5.5
2018-10-26	12:41:14	8.5
2018-10-26	16:07:10	8.5
2018-10-30	03:00:00	13.0
2018-10-30	08:32:26	17.5
2018-11-01	03:44:49	7.0
2018-11-04	03:12:46	3.0
2018-11-05	06:46:13	5.0
2018-11-11	23:38:35	5.0
2018-11-12	06:50:29	13.0
2018-11-15	09:02:06	8.5
2018-11-15	09:09:27	8.5
2018-11-19	13:05:56	11.0
2018-12-25	01:41:28	8.5
2019-03-17	11:49:40	7.0
2019-05-13	16:57:17	8.5

Table S6. Table summarising the contribution of the various seismic and/or aseismic processes to the overall plate-convergence strain budget. See text for discussion.

Process captured	Slip rate (mm/yr)	% of total convergence rate (26 mm/yr)
Interseismic velocity between Zakynthos/western Peloponnese	21.4	-
Microseismicity	1.3	5
SSEs	2.1	8
Strain released due to seismic/aseismic deformation	3.4	13
Strain stored elastically in the crust	18	69

Movie S1. Evolution in map-view and cross section (along the transect A-B) of the monthly seismic moment distribution, and equivalent M_w , within the study area. Grey contours in map view and cross section mark the top of the plate-interface (Halpaap et al., 2019). Highlighted with blue contours mark the map-view extent of the transient signal. Inset: timeline indicating the two transient signals (blue rectangles) in 2014 and 2018. See text in the main article for details.

Movie S2. Green arrows and ellipses indicate the daily displacements and respective errors of the GNSS stations. Magenta arrows indicate the daily displacements and respective errors predicted by fluid loading. Scale is shown with the black arrow at the bottom of the plot. Velocities and errors have been estimated from the GNSS and fluid loading displacement time series by using the GrAtSiD algorithm (Bedford and Bevis, 2018) that models trajectories. Displacements shown in this animation are taken from the averaged trajectory model minus the background seasonal oscillation (Fourier terms). Earthquakes from the ZES are plotted as red circles with radius corresponding to the scale (bottom left).

Movie S3. Evolution of the daily velocities of the transient GPS signal with respect to the long-term velocity of each station.

References for the Supplementary Information

Aki, K., 1966. Generation and Propagation of G Waves from the Niigata Earthquake of June 16, 1964.: Part 2. Estimation of earthquake moment, released energy, and stress-strain drop from the G wave spectrum. *Bull. Earthquake Res. Inst., University of Tokyo*, 44, 73-88.

Albuquerque Seismological Laboratory (ASL)/USGS, 1988. Global Seismograph Network - IRIS/USGS. International Federation of Digital Seismograph Networks. Dataset/Seismic Network. 10.7914/SN/IU

AUTH (Aristotle University of Thessaloniki), 1981. Aristotle University of Thessaloniki Seismological Network. International Federation of Digital Seismograph Networks. 10.7914/SN/HT, <https://doi.org/10.7914/SN/HT>.

Bedford, J., Bevis, M., 2018. Greedy automatic signal decomposition and its application to daily GPS time series, *J. Geophys. Res.* 123, B014765, 6992–7003.

Cesca, S., Heimann, S., Stammer, K., Dahm, T., 2010. Automated procedure for point and kinematic source inversion at regional distances. *J. Geophys. Res.*, 115, doi:10.1029/2009JB006450

Cesca, S., Rohr, A., Dahm, T. 2013. Discrimination of induced seismicity by full moment tensor inversion and decomposition. *J. Seismol.* 17, 1, 147-163, doi:10.1007/s10950-012-9305-8

Cesca, S., 2020. Seiscloud, a tool for density-based seismicity clustering and visualization. *J. Seismol.* <https://doi.org/10.1007/s10950-020-09921-8>

GEOFON Data Centre, 1993. *GEOFON Seismic Network*. Deutsches GeoForschungsZentrum GFZ. <https://doi.org/10.14470/TR560404>

Grigoli, F., Cesca, S., Rinaldi, A. P., Manconi, A., Lopez Comino, J. A., Clinton, J. F., Westaway, R., Cauzzi, C., Dahm, T., Wiemer, S., 2018. The November 2017 Mw 5.5 Pohang earthquake: A possible case of induced seismicity in South Korea, *Science* 360, 6392, 1003-1006, doi:10.1126/science.aat2010.

Haddad, A., Ganas, A., Kassaras, I., Lupi, M., 2020. Seismicity and geodynamics of western Peloponnese and central Ionian Islands: insights from a local seismic deployment, *Tectonophysics*, <https://doi.org/10.1016/j.tecto.2020.228353>.

Halpaap, F., Rondenay, S., Perrin, A., Goes, S., Ottemöller, L., Austrheim, H.O., Shaw, R., Eeken, T., 2019. Earthquakes track subduction fluids from slab source to mantle wedge sink. *Sci. Adv.* 5, doi: 10.1126/sciadv.aav7369.

Hanks, T.C., Kanamori, H., 1979. A moment magnitude scale. *J. Geophys. Res.* 84, 2348-2350.

Heimann, S., Isken, M., Kühn, D., Sudhaus, H., Steinberg, A., Vasyura-Bathke, H., Daout, S., Cesca, S., Dahm, T., 2018. Grond - A probabilistic earthquake source inversion framework. V. 1.0. GFZ Data Services. <https://doi.org/10.5880/GFZ.2.1.2018.003>

INGV Seismological Data Centre, 2006. *Rete Sismica Nazionale (RSN)*. Istituto Nazionale di Geofisica e Vulcanologia (INGV), Italy. <https://doi.org/10.13127/SD/X0FXNH7QFY>

INGV (Istituto Nazionale di Geofisica e Vulcanologia), 2009. Emersito Seismic Network for Site Effect Studies in L'Aquila town (Central Italy). International Federation of Digital Seismograph Networks. Dataset/Seismic Network. 10.7914/SN/4A_2009

Institute of Geosciences, Energy, Water and Environment, 2002. Albanian Seismological Network. International Federation of Digital Seismograph Networks. Dataset/Seismic Network. 10.7914/SN/AC

Institut De Physique Du Globe De Paris (IPGP), & Ecole Et Observatoire Des Sciences De La Terre De Strasbourg (EOST), 1982. *GEOSCOPE, French Global Network of broad band seismic stations*. Institut de Physique du Globe de Paris (IPGP). <https://doi.org/10.18715/GEOSCOPE.G>

Kassaras, I., Kapetanidis, V., Karakonstantis, A., 2016. On the spatial distribution of seismicity and the 3D tectonic stress field in western Greece. *Phys. Chem. Earth.* 95, 50-72.

Lomax, A., Michelini, A., Curtis, A., 2009. Earthquake Location, Direct, Global-Search Methods, in: Meyers, R.A. (Ed.), *Encyclopedia of Complexity and Systems Science*. Springer New York, New York, NY, pp. 2449–2473.

Lomax, A., Virieux, J., Volant, P., Berge-Thierry, C., 2000. Probabilistic earthquake location in 3D and layered models, in: Thurber, C.H., Rabinowitz, N. (Eds.), *Advances in Seismic Event Location*. Springer, Dordrecht, Kluwer, Amsterdam, pp. 101–134.

MedNet Project Partner Institutions, 1990. *Mediterranean Very Broadband Seismographic Network (MedNet)*. Istituto Nazionale di Geofisica e Vulcanologia (INGV). <https://doi.org/10.13127/SD/FBBBTDTD6Q>

NOA (National Observatory of Athens), Institute of Geodynamics, Athens, 1997. National Observatory of Athens Seismic Network. International Federation of Digital Seismograph Networks. Dataset/Seismic Network. 10.7914/SN/HL, <https://doi.org/10.7914/SN/HL>.

Negi, S. S., Paul, A., Cesca, S., Kamal, Kriegerowski, M., Mahesh, P., Gupta, S., 2017. Crustal velocity structure and earthquake processes of Garhwal-Kumaun Himalaya: Constraints from regional waveform inversion and array beam modeling, *Tectonophysics* 712, 45-63, doi:10.1016/j.tecto.2017.05.007

NOA (National Observatory of Athens), Institute of Geodynamics, Athens, 1997. National Observatory of Athens Seismic Network. International Federation of Digital Seismograph Networks. Dataset/Seismic Network, <https://doi.org/10.7914/SN/HL>.

Okada, Y., 1985. Surface deformation due shear and tensile faults in a half-space. *Bull. Seismol. Soc. Am.* 75, 1135–1154.

Pearce, D., Rondenay, S., Sachpazi, M., Charalampakis, M., Royden, L.H., 2012. Seismic investigation of the transition from continental to oceanic subduction along the western Hellenic subduction Zone. *J. Geophys. Res.* 117, 1–18. <https://doi.org/10.1029/2011JB009023>

Pérouse, E., Sébrier, M., Braucher, R., Chamot-Rooke, N., Bourlès, D., Briole, P., Sorel, D., Dimitrov, D., Arsenikos, S., 2017. Transition from collision to subduction in Western Greece: the Katouna–Stamna active fault system and regional kinematics. *Intern. J. Earth Sci.* 106, 967–989, doi:10.1007/s00531-016-1345-9.

Scripps Institution of Oceanography, 1986. Global Seismograph Network - IRIS/IDA. International Federation of Digital Seismograph Networks. Dataset/Seismic Network. 10.7914/SN/II

Sokos, E., 2015. Lefkada temporary network. International Federation of Digital Seismograph Networks. Dataset/Seismic Network. 10.7914/SN/X5_2015

Sokos, E., Gallovič, F., Evangelidis, C. P., Serpetsidaki, A., Plicka, V., Kostelecký, J., Zahradník, J., 2020. The 2018 Mw 6.8 Zakynthos, Greece, Earthquake: Dominant Strike-Slip Faulting near Subducting Slab, *Seismol. Res. Lett.*, doi:10.1785/0220190169

UA (University of Athens), 2008. Hellenic Seismological Network, University of Athens, Seismological Laboratory. International Federation of Digital Seismograph Networks. Dataset/Seismic Network. 10.7914/SN/HA

UP (University of Patras), 2000. University of Patras, Seismological Laboratory. International Federation of Digital Seismograph Networks. Dataset/Seismic Network. 10.7914/SN/HP

Utsu T., 1965. A method for determining the value of b in a formula $329 \log n = a - bM$ showing the magnitude-frequency relation for 330 earthquakes. *Geophys. Bull., Hokkaido Univ.* 13, 99–103.

Wiemer, S., Wyss, M., 2000. Minimum magnitude of completeness in earthquake catalogs: Examples from Alaska, the Western United States, and Japan. *Bull. Seismol. Soc. Am.* 90, 859–869.